2010

PREPARATION AND CHARACTERIZATION OF SELFASSEMBLED UNILAMELLAR VESICLES FOR CONTROLLED RELEASE

Suanne Sarah Mahabir
Western University

PREPARATION AND CHARACTERIZATION OF SELF-ASSEMBLED UNILAMELLAR VESICLES FOR CONTROLLED RELEASE

(Spine Title: Self-Assembled Unilamellar Vesicles)

(Thesis format: Monograph)

by

Suanne Sarah Mahabir

Graduate Program in Biomedical Engineering

A thesis submitted in partial fulfilment
of the requirements for the degree of
Master of Engineering Science

The School of Graduate and Postdoctoral Studies
The University of Western Ontario
London, Ontario, Canada

THE UNIVERSITY OF WESTERN ONTARIO
SCHOOL OF GRADUATE AND POSTDOCTORAL STUDIES

CERTIFICATE OF EXAMINATION

Supervisor

Dr. Wankei Wan

Supervisory Committee

Dr. Beth Gillies

Dr. Jeff Hutter

Dr. Mac Quantz

Examiners

Dr. John de Bruyn

Dr. Don Hewson

Dr. Jeff Hutter

The thesis by

Suanne Sarah Mahabir

entitled:

Preparation and Characterization of Self-Assembled Unilamellar Vesicles for Controlled Release

is accepted in partial fulfillment of the
requirements for the degree of
Master of Engineering Science

Date_____

_____
Chair of the Thesis Examination Board

ABSTRACT

Unilamellar vesicles (ULVs) are effective drug delivery vehicles used to encapsulate therapeutic agents. Growing interest of their use in the pharmaceutical sciences is a result of their reported ability to enhance therapeutic efficacy at low doses, increase the half life of administered agents, and provide site targeted delivery. Since their initial synthesis in 1965 by Bangham et al., a variety of methods for producing ULVs have been proposed and investigated. Recently, a spontaneously forming ULV was reported using a combination of natural phospholipids: dimyristoyl-phosphatidylcholine (DMPC), dimyristoyl-phosphatidylglycerol (DMPG) and dihexanoyl-phosphatidylcholine (DHPC). This system offers great potential as a controlled release system due to its finite size control, narrow size distribution, batch-to-batch reproducibility, ease of preparation and shelf life stability. This research focuses on (1) the ability to form these ULVs and characterize them using small-angle neutron scattering (SANS) and cryogenic transmission electron microscopy (cryo-TEM); (2) the ability to control their size and size distribution by varying charge density, total lipid concentration, and annealing rate; (3) the stability of these ULVs once formed with respect to dilution factor and (4) the precursor bicelle structure, its growth, and role in the end-state vesicle. The spontaneous formation of ULVs was successfully identified using both SANS and cryo-TEM. Results indicated that they existed only within a narrow window of charge densities, where larger size ULVs could be obtained at a lower charge density through slow temperature annealing. By varying the annealing rate and charge density, a six-fold change in mean radius of the ULVs was observed. The time-resolved bicelle experiments showed that the size of the nano-disks increased continuously due to disk interactions where their coalescence was best described

by a power law relationship with time. Overall, the growth rate increased with increasing temperature and ionic strength and decreased with total lipid concentration, whereas the size of the end-state ULV increased with increasing annealing temperature, ionic strength and total lipid concentration. Finally, the stability of these ULVs was confirmed through a series of high temperature dilution experiments. This work contributes to the basic understanding of ULV formation, methods of controlling the size and stability offering insight for applications as a potential nano-carrier system.

Keywords: Drug delivery, Unilamellar vesicles, spontaneously forming (self-assembled), low polydispersity, bicelles, small angle neutron scattering (SANS), cryogenic transmission electron microscopy (cryo-TEM), charge density, kinetic study, annealing rate

ACKNOWLEDGEMENTS

I would like to express my sincere gratitude to my supervisors Dr. Wankei Wan and Dr. Mu-Ping Nieh for their guidance and encouragement throughout this work. I am very appreciative of their ongoing support and insightful suggestions and discussions during the development of this thesis. Their invaluable expertise, knowledge and advice have made this a memorable learning experience for me.

I would also like to thank my colleagues (D. Daniher, G. Guhados, K. Kennedy, E. Lee, M. Mekhail, L. Millon, A. Norman, C. Oates, D. Padavan, D. Small, M. Spaic, E. Wong and K. Wong) who have all been instrumental in facilitating portions of this work through their technical advice and valuable friendships. In particular I would like to thank Donna Padavan for her on-going help and thesis revisions.

Much of this work would not have been possible without the technical expertise of Dr. John Katsaras (Canadian Neutron Beam Centre), Stephen Hudson (Department of Physics and Astronomy), Dr. Steven Kline (National Institute of Standards and Technology), Drs. Ken Littrell and Lisa Debeer-Schmitt (Oak Ridge National Lab) and Robert Harris (University of Guelph).

Furthermore, I would like to acknowledge the Canadian Institute of Health Research (CIHR), Ontario government (OGS) and The University of Western Ontario (WGRS) for their financial support during these studies. I would also like to acknowledge the Canadian Institute of Neutron Scattering (CINS) and the Canadian Neutron Beam Centre (CNBC) for their financial support in facilitating visits to various beam centres throughout this research.

My family and friends deserve a special thank you for their unconditional love, encouragement and support over the past years, leading up to and during this work.

TABLE OF CONTENTS

LIST OF FIGURES

CHAPTER 5

CHAPTER 6

LIST OF TABLES

ABBREVIATIONS

$A_{vesicle}$	Inner and outer surface area of vesicle
A_{disk}	Total surface area fo disk
C_{lp}	Total lipid concentration
cryo-TEM	Cryogenic transmission electron microscopy
CMC	Critical micelle concentration
d	Diameter
D	Dimension
D_2O	Deuterium Oxide
DHPC	Dihexanoyl phosphatidylcholine
DMPC	Dimyristoyl phosphatidylcholine
DMPG	Dimyristoyl phosphatidylglycerol
EPR	Enhanced Permeation and Retention
$f(r)$	The Schulz distribution function
$F(q)$	Form factor
hr	hour
I_{inc}	Incoherent scattering
$I(q)$	Scattered intensity
$J_1(x)$	First order Bessel function
L	Hydrophobic disk thickness
MLVs	Multilamellar vesicles
MPS	Mononuclear phagocyte system
n	Number particle density
NaCl	Sodium chloride
NCNR	NIST Center for Neutron Research
NIST	National Institute of Standards and Technology
ORNL	Oak Ridge National Lab
p	Polydispersity (standard deviation/average vesicle radius)
PEG	Poly(ethylene glycol)
q	scattering vector
R	Radius of hydrophobic disk core

R_i	Inner ULV radius
R_o; R_v	Outer ULV radius ($R_i + t_{bilayer}$)
R_1	Initial disk size in kinetic study
SANS	Small-angle neutron scattering
SDD	Sample-to-detector distances
SLD	Scattering length density
$S(q)$	Structure Factor
t	Disks hydrophilic shell thickness
$t_{bilayer}$	Vesicle bilayer thickness
T	Temperature
T_c	Critical phase transition temperature of DMPC (23 °C)
T-jump	Temperature jump from 10 to 50 °C
ULV	Unilamellar Vesicle
$V_{hydrophilic}$	Volume of the hydrophilic shell [$=\pi(R+t)^2(L+2t)$]
$V_{hydrophobic}$	Volume of the hydrophobic core ($=\pi R^2 L$)
$V_{vesicle}$	Total ULV volume
α	the angle between the cylinder axis and the scattering vector, q
$\Gamma(1/p^2)$	Gamma function
θ	scattering angle
$\rho_{hydrophilic}$	SLD disk's shell
$\rho_{hydrophobic}$	SLD disk's core
ρ_{lipid}	Uniform SLD for $\rho_{hydrophilic}$ and $\rho_{hydrophobic}$
$\rho_{solvent}$	SLD of solvent (D_2O)
σ^2	Variance
ϕ_{lipid}	Lipid volume fraction

CHAPTER 1
INTRODUCTION

1.1 OVERVIEW

For a therapeutic molecule to be effective in the treatment of a specific disease, it has to be delivered to the site where it is needed. At the same time, there is also a need to control undesired drug action in healthy tissues and to minimize negative side effects. One method for delivery involves the use of carriers, some of which include proteins, immunoglobulins, synthetic polymers and/or unilamellar vesicles (ULVs) [1-3]. Over the years, a lot of effort has been expended in the design of delivery systems. Of particular interest are the phospholipid based liposomes known as ULVs. ULVs are spheres comprised of a single shell lipid bilayer surrounding an aqueous core. The compounds to be delivered are typically entrapped inside the ULV core. The lipid shell offers protection to its contents from exposure to the environment and is reported to prevent rapid degradation (by enzymes), allow retention of activity (avoid exposure to inhibitors) and minimize side effects. Efforts have also been made to impart specificity to this class of drug carrier to target organs, cells or compartments within the cells, demonstrating the potential for improving drug therapies using this technology [1, 3, 4].

Several methods for the preparation of large ULVs (on the order of microns) exist. One of the most common methods used is solvent dispersion (i.e., reverse phase evaporation or double emulsion). However, for applications in drug delivery, smaller ULVs (diameter < 200 nm) are known to be more effective [5]. In another common approach, ULVs are obtained from the breakdown of multilamellar vesicles (MLVs) using mechanical methods, the most common being extrusion [5-7]. One of the major drawbacks associated with these techniques is the high polydispersity of the resulting product.

Furthermore, degradation, modification of phospholipids (i.e., oxidation, hydrolysis, denaturation) and low throughput are also concerns [8]. Spontaneously forming ULVs were first introduced through detergent removal techniques using micellar solutions [9]; however, detergent contamination was thought to compromise their biocompatibility. In addition, difficulty in controlling ULVs' size was reported and seen as a limitation [10].

More recently, a self assembling vesicular system composed of natural phospholipids dissolved in aqueous solution was reported [11, 12]. This system was comprised of two long chain lipids - dimyristoyl-phosphatidylcholine (DMPC) and dimyristoyl-phosphatidylglycerol (DMPG) and a short chain lipid - dihexanoyl-phosphatidylcholine (DHPC) [13, 14]. Bicelles (disk-like structures) are the precursor structures to the spontaneously formed ULVs. The bicelle-to-vesicle transformation is described by a three step process [15, 16]:

(1) Uniform growth of disks by coalescence with neighboring disks above a critical temperature, $T_c \sim 23$ °C.
(2) Instability of disks resulting from insufficient rim coverage with short-chain lipid. (3) Disk closure to form stable ULVs.

Results of studies so far indicate that this system forms stable, low polydispersity ULVs at low lipid concentrations (< 2 wt.%) and above T_c (~ 23°C) where dilution factor, charge density, lipid molar ratio and ionic strength are controlling factors of the end-state ULVs [12, 14, 15, 17]. Moreover, DMPC/DMPG/DHPC ULVs at total lipid concentrations, $C_{lp} \leq 0.33$ wt.% are stable for up to four months at 4 °C, and a few weeks at 45 °C [14, 18]. These ULVs demonstrated two temperature dependent release mechanisms, making them suitable candidates for drug delivery applications [19].

In this thesis, we aim to further understand how composition and processing parameters affect ULV formation.

1.2 THESIS OBJECTIVES

1. To characterize spontaneously formed unilamellar vesicles using small-angle neutron scattering (SANS) and cryogenic transmission electron microscopy (cryo-TEM).

2. To study the effect of composition and processing condition on the size and polydispersity of the ULVs formed. Specifically the influence of charge density and heating rate on ULV formation are investigated.

3. To investigate the stability of monodisperse ULVs following high temperature dilution to simulate the effects of intravenous drug delivery.

4. To quantify low temperature bicelle growth kinetics as a function of total lipid concentration, ionic strength and temperature ($T < T_c$), and investigate the effects of bicelle growth on the characteristics of the end-state ULVs using SANS.

1.3 THESIS OUTLINE

The work outlined in this thesis focuses on the formation and the characterization of unilamellar vesicles. This thesis is divided into 7 chapters.

Chapter 2 is a detailed literature review focusing on vesicular systems for controlled release applications, conventional methods of production, limitations associated with current methods, self-assembled ULVs and SANS as a characterization tool.

Chapter 3 lists the materials, outlines the ULV formation parameters and procedures and comments on the principles and parameters of the analytical tools used to characterize them.

Chapter 4 focuses on the results on thevesicle confirmation and characterization using small-angle neutron scattering and transmission electron microscopy.

Chapter 5 focuses on the results and discussion on the parameter optimization and stability study.

Chapter 6 focuses on the results and discussion on the kinetic study of bicelle growth and end-state ULVs.

Chapters 7 summarizes the significance, contributions, conclusions, recommendations and possible future directions of this research.

CHAPTER 2
LITERATURE REVIEW

2.1 IMPORTANCE OF DRUG DELIVERY SYSTEMS IN THERAPY

The therapeutic efficacy of a drug demonstrated *in vitro* is often followed by reduced effects upon delivery *in vivo*. Mehnert and Mader identified the following limitations associated with free drug treatment methods: poor absorption, rapid elimination, biodistribution throughout the body, and toxic effects [20]. Drug delivery devices are important in overcoming some of the above mentioned problems where they are designed to increase the therapeutic efficacy while minimizing side effects. Summarized in Table 2.1.1 are some of the problems exhibited by free drugs that can be reduced by using carefully designed drug delivery devices. These systems span a wide range of applications from controlled release wound dressings to controlled release scaffolds for tissue regeneration to larger scale drug releasing implants [2, 3]. Drug delivery devices can be made from a variety of materials including synthetic and natural; degradable and non-degradable; organic, inorganic or metallic materials. There also exists a range of stimuli-responsive materials which are designed to release the encapsulated agents upon changes to the surrounding environmental conditions such as pH and temperature [2].

The work described in this thesis is focused on the development of a small, nanometer scale delivery system, where such systems are best known for their high surface area to volume ratio, ability to target specific regions of the body and ability to permeate through cell membranes. Specifically we will focus on liposomes.

Table 2.1.1. Undesired properties of free drugs, their implications and potential improvements through the use of drug delivery devices [3].

Problems and Implications	**Improvements Offered by Drug Delivery Systems**
POOR SOLUBILITY	
Hydrophobic drugs may precipitate in aqueous media and toxicities are associated with the use of excipients	Lipid micelles or liposomes provide both hydrophilic and hydrophobic environments improving drug solubility
TISSUE DAMAGE	
Cytotoxic drugs leads to tissue damage (i.e. tissue necrosis seen with free anti-cancer drugs)	Regulated drug release can reduce or eliminate tissue damage
RAPID BREAKDOWN IN VIVO	
Loss of activity of the drug following administration (i.e. due to physiological temperatures or pH)	Drug delivery systems can protect the drug from premature or rapid degradation and introduce functions of sustained release, resulting in lower dose requirements
UNFAVORABLE PHARMACOKINETICS	
Drug is cleared rapidly by the kidney requiring high doses or continuous infusion to counteract effects	Devices can alter the pharmacokinetics of the system by reducing clearance
POOR BIODISTRIBUTION	
Drugs that have widespread distribution in the body can affect normal tissue resulting in dose-limiting side effects such as cardiac toxicity	Systems can reduce the volume of distribution and help reduce side effects in sensitive non-target tissue through site targeted delivery
LACK OF SELECTIVITY FOR TARGET TISSUES	
Distribution of the drug to normal tissue leads to side effects that restrict the amount of drug that can be administered. Low concentrations in target tissue result in suboptimal therapeutic effects	Can be used to increase drug concentrations in diseased tissues such as tumors or through ligand-mediated targeting

2.2 LIPOSOMES AS AN EFFECTIVE DELIVERY SYSTEM

Liposomes including multilamellar vesicles (MLVs) and unilamellar vesicles (ULVs) are formed by dissolving natural phospholipids in aqueous solution. First reported by Bangham et al., MLVs have an onion-like structure and are composed of concentric lipid bilayers, with diameters between 1 – 5 μm. ULVs comprised of a single lipid bilayer and

ranging in diameters from 50 – 250 nm are of greater interest in the pharmaceutical sciences. Their large aqueous core makes them ideal for entrapping water-soluble agents while their lipid bilayer makes them capable of incorporating hydrophobic agents for delivery. Advantageous characteristics of ULVs include biocompatibility, biodegradability, low toxicity and variability of structure. Interest in ULVs as viable carriers of therapeutic agents, image contrasting agents, genes, etc. is currently on the rise [8, 21]. They act by protecting encapsulated molecules from degradation and by creating an ability to passively target tissues or organs that have a discontinuous endothelium, such as the liver, spleen, bone marrow, etc. [21]. Selective delivery is demonstrated by functionalization of the vesicle wall with site specific ligands (i.e., antibodies, apoproteins and/or hormones). This offers specific drug action in targeted locations such as organs, cellular subsets or intramuscular regions through recognition of specific receptors at the targeted sites. Ultimately this prevents free flow of the compound throughout the body upon delivery – minimizing side effects, increasing dose effectiveness by reducing non-specific uptake, and possibly delivering to regions that may not be easily treatable [3, 8].

2.3 Current Examples Of Applications Of ULVs

Currently, several ULV systems are commercially available; some examples are presented in Table 2.3.1. One of the early applications is Doxil, which is used for the delivery of the toxic anti-cancer agent Doxorubicin. This system is used to treat various forms of cancer including Kaposi's sarcoma, ovarian, breast, prostate and liver cancer. It is composed of phospholipids conjugated with poly-(ethylene-glycol) (PEG) with average vesicle diameters of 80-90 nm and a high polydispersity (broad size distribution) [22]. The effectiveness of this system is associated with 1) the functionalization of the surface with PEG, creating a long-circulating time system and 2) alterations in the biodistribution due to a mechanism known as the enhanced permeability and retention (EPR) effect, seen in solid tumors and inflamed tissues. Functionalization of the vesicle surface with an inert molecule (in this case PEG) creates a spatial barrier, introducing steric hindrance and preventing interactions between the vesicle wall and other macromolecules. This blocked access to the vesicle surface suppresses particle

recognition, reducing non-specific uptake [23]. EPR is a pathological condition where the permeability of the tissue vasculature increases to the point that particulate carriers are able to localize in these areas. As tumors grow and outstrip the supply of the oxygen and nutrients, they release cytokines and other signaling molecules that recruit new blood vessels to the tumor in a process called angiogenesis [24, 25]. Unlike tight blood vessels in normal tissue, this type of tumor-induced blood vessels have gaps as large as 600 to 800 nm between adjacent endothelial cells through which ULVs can enter and concentrate in the tumor interstitial space. Large increases in tumor drug concentrations (10-fold higher) are reported relative to administration with the free drug alone [3, 26]. Moreover, this results in a reduction in toxicity to healthy tissues; specifically at the site of injection and to the heart [22].

Table 2.3.1. Examples of approved vesicular formulations for commercial use [21].

Product name (active agent)	**Company, year of product marketing**	**Application**
Doxil (doxorubicin)	Sequus pharmaceuticals, 1997	Kaposi's sarcoma
DaunoXome (daunorubicin)	Nexstar Pharmaceuticals, 1995	Kaposi's sarcoma
Myocet/Evacet (doxorubicin)	Elan Pharma, 2000	Metastatic breast cancer
Depocyt (cytarabine)	SkyePharma, 1999	Lymphomatous meningitis
Ambisome (ampotericin)	Fujisawa USA Inc. and Nexstar Pharm 1997	Fungal infections in immuno-compromised patients

2.4 Size And Polydispersity Control Of ULVs

Modulating the size and polydispersity of the ULVs is important in reducing non-specific uptake by the mononuclear phagocyte system (MPS) in which large ULVs are eliminated from the blood circulation more rapidly than small ULVs; reducing circulation time and consequently therapeutic effectiveness [27]. Desired uptake by targeted cells and regions is also shown to be size dependent. Chithrani et al. indicated cells to have a preference for particles with diameters of 50 nm with reduced uptake with larger (74 and 100 nm) sizes [28]. Another study investigated the size dependence of tumor uptake for ULVs of varying size. They reported penetration and accumulation of PEG modified ULVs of up

to 400 nm diameter where tumor vessels are known for the EPR effect [29]. Controlling the mean size is known to affect the tissue distribution *in vivo*, *in vivo* circulation lifetimes, and transfer of lipids into cells. In addition, a large emphasis is placed on controlling the size distribution of ULVs as it affects the encapsulation efficiency, and therapeutic effectiveness [8].

2.5 METHODS FOR ULV FORMATION AND THEIR LIMITATIONS

2.5.1 Mechanical Methods

Bangham et al. were the first to prepare vesicles from animal based phospholipids (phosphatidyl choline extracted from hens' eggs). These were dissolved in chloroform under nitrogen followed by evaporation under a vacuum. The suspension was then hydrated using water, followed by vigorous shaking, leading to the formation of vesicles. They found that if the suspension was hydrated with liquid containing a therapeutic agent, it was possible to entrap the agent into the vesicle [30]. The physical properties of these vesicles were examined using electron microscopy by which a wide size distribution of MLVs was identified (diameter > 1μm) [31]. This technique introduced breakthrough technology in the synthesis of vesicles; however MLVs are ineffective drug delivery vehicles due to the large size and size distribution, leading to rapid clearance from the body and the multiple bilayer membranes which limit encapsulation efficiency. Consequently, methods for breaking down MLVs into ULVs were investigated using mechanical methods.

Johnson et al. described the formation of ULVs from MLVs using sonication. They took the lipid suspension created by Bangham et al. and exposed it to pulsed, high frequency sound waves to agitate the suspension of MLVs. This was done under nitrogen for ~0.5 to 1.5 hours in a temperature controlled environment. Transmission electron microscopy on stained ULVs revealed the breakdown of MLVs into single bilayer shells with diameters ranging between 50 nm to 250 nm [31].

A more common approach is the use of multi-stage extrusion for breaking down MLVs. This involves pushing the solution of MLVs (prepared using the conventional method) repeatedly through a series of polycarbonate membranes with pores which range in diameters between 0.05-1 μm [10]. This method requires a reduced lipid concentration (10-12 μmol/ml) before being pushed through the membranes. Typically a series of membranes starting with the largest pore diameter and ending with the smallest are used (i.e., 1, 0.8, 0.6, 0.4 and 0.2 μm). The sequential extrusion reduces the mean size and size heterogeneity of the ULVs [6, 10]. Berger et al. report a mean size between 20 – 100 nm and a narrower size distribution compared to the sonication method following 6 extrusions.

The use of sonication exposes the vesicles to mechanical stress in water, potentially leading to oxidation or hydrolysis of the fatty acid chains in the phospholipid tails or denaturation or inactivation of some substances that are to be encapsulated. In addition this method requires multiple steps, high energy and results in the formation of fairly polydisperse samples [8]. Extrusion is capable of producing ULVs of a narrow size distribution however is still considered to be a labor intensive method that can be problematic for the production of smaller ULVs ($d < 50$ nm) and is limited by membrane fouling [8, 15].

2.5.2 Solvent Dispersion Methods

Unlike the previously mentioned mechanical methods, solvent dispersion methods typically produce single shelled vesicles without the need to first form MLVs. These methods include reverse-phase evaporation and the double emulsion technique, typically producing vesicles 100 nm - 1 μm which are larger in size with a wider size distribution. These procedures require the use of strong solvents such as methanol, ethanol, ether (diethyl, isopropyl, petroleum), hexane, benzene and chloroform, dichloromethane or other hydrocarbons for dissolving lipids, thus introducing limitations of biocompatibility [8]. In addition they often require sonication and mechanical agitation which introduces harmful shear forces which pose a threat to any sensitive encapsulated materials such as proteins and/or DNA which could be denatured. Depending on the formulation used, the

stability, size and size distribution of ULVs formed will vary. Shear stresses can be used to decrease the droplet size and droplet size distribution, increasing the frequency of collision and coalescence of internal droplets with the outer water phase [32]. Another method for controlling the size is by varying the ratio of solvent to water during the vesicle formation process or by varying the solvent itself. Ishii et al. demonstrated the role of solvent boiling point on the size of vesicles formed. Overall, solvents with higher boiling points (*n*-hexane and benzene) formed larger vesicles than solvents with lower boiling points (diethyl ether). They reported ULVs in the size range from 175 nm to 300 nm in diameter depending on the solvent [33].

2.5.3 Limitations with Conventional Methods of Production

While ULVs have been demonstrated to be an effective delivery mechanism and are used in the pharmaceutical industry today, their widespread use is limited by a number of problems [8]. These include:

1. Direct ULV formation
2. Difficulties in controlling liposome size
3. Difficulties in controlling liposome size distribution
4. The use of organic solvents
5. Difficulties in process scale-up
6. Limited shelf life stability
7. Poor batch-to-batch reproducibility

2.6 Self-Assembled ULVs

One approach to simplify ULV preparation is direct formation, avoiding the MLV step. This can be achieved by a spontaneous formation route. The first success of spontaneously forming ULVs was reported with the use of cationic/anionic surfactants with vesiculation reported following a series of dilutions and/or temperature jumps [34-37]. However, aside from the use of surfactants, these self assembling systems were limited by the fact that the size was directly related to surfactant concentration [38]. This created a non-ideal situation for drug delivery applications considering that upon

injection into the body, the ULVs risked bursting, prematurely releasing encapsulated materials.

More recently, Nieh et al. reported a novel approach towards the formation of self-assembled ULVs composed entirely of phospholipids, in the absence of surfactants and having the advantage of size stability independent of lipid concentration [13, 14]. In general, a combination of neutral and charged long-chain lipids and neutral short-chain lipids are used to form ULVs as a function of total lipid concentration and temperature. This system is formed using the long-chain lipids dimyristoyl phosphatidylcholine (DMPC), dimyristoyl phosphatidylglycerol (DMPG) and the short-chain lipid dihexanoyl phosphatidylcholine (DHPC). Small-angle neutron scattering (SANS) was used to confirm that this system is able to form small ULVs (diameters < 50 nm), with a narrow size distribution (polydispersity < 0.3) under dilute conditions and at temperatures greater than the main phase transition temperature of DMPC (T_c ~ 23°C). The spontaneous formation of these ULVs is a function of (1) temperature, (2) total lipid concentration, (3) the long-to-short chain lipid molar ratio, and (4) charge density, offering control of ULV synthesis through variation of several basic experimental parameters [13]. Importantly, ULV stability is reported over periods of months at 45 °C [39] and furthermore controlled release studies demonstrated no release of encapsulated materials around normal body temperature (~32 – 45 °C) indicating initial stability upon injection [19]. In summary, the formation of these ULVs is reported to be advantageous due to their ease of preparation, good size uniformity and reproducibility, high stability over time and from the absence of contamination with MLVs.

2.6.1 ULV Formation Mechanism

ULVs are formed from a precursor disk-like micelle, also known as a bicelle. The disks become unstable at a critical point and fold into vesicles [16, 40]. The low-temperature bicelle phase in this system has been verified by SANS experiments [12]. Each of the phospholipids in the mixture plays an important role in stabilizing this bicelle phase. DMPC, a zwitterionic, long chain (14:0 hydrocarbon chain) phospholipid, forms the bulk of the rigid planar structure (the face) in the bilayer; DHPC, a zwitterionic, short chain

(6:0 hydrocarbon chain) phospholipid, sits on the edge of the disk, stabilizing it by minimizing the energy due to the rims' high curvature and potential exposure of DMPCs' hydrophobic tails to water; DMPG, a negatively charged, long chain (14:0 hydrocarbon chain) phospholipid, stabilizes the lamellar phase and prevents the separation of the short chain (DHPC) from the long chain (DMPC) lipid and also introduces repulsive forces between the disks, preventing face-to-face interaction which would result in MLV formation [12].

A conceptual phase diagram representing this system is shown in Figure 2.6.1.1 in which various structures are outlined as a function of temperature and total lipid concentration. Bicelles exist at low temperatures (< 23 °C), ULVs at low lipid concentrations, and MLVs at higher lipid concentrations and temperatures. The phase transition temperature of DMPC ($T_c \sim 23$ °C) is important in the formation of ULVs [41]. Figure 2.6.1.2 depicts the mechanism in which bicelles transform into ULVs. In the low temperature phase, bicelles become unstable around 23 °C where DMPC's acyl chains melt, resulting in increased miscibility with DHPC. This leads to a loss of DHPC at the disk rims by allowing some of it to enter into the DMPC rich planar region. To minimize this loss of stability and exposure of the hydrophobic chains, the disks begin to coalesce with neighbouring disks forming larger sized bicelles where at a critical point the disk becomes unstable causing them to fold into vesicles [12]. From this description it can be noted that the spontaneous formation of ULVs is path dependent in which the precursor bicelle formation is critical. The path of formation is outlined by the black arrows in Figure 2.6.1.1.

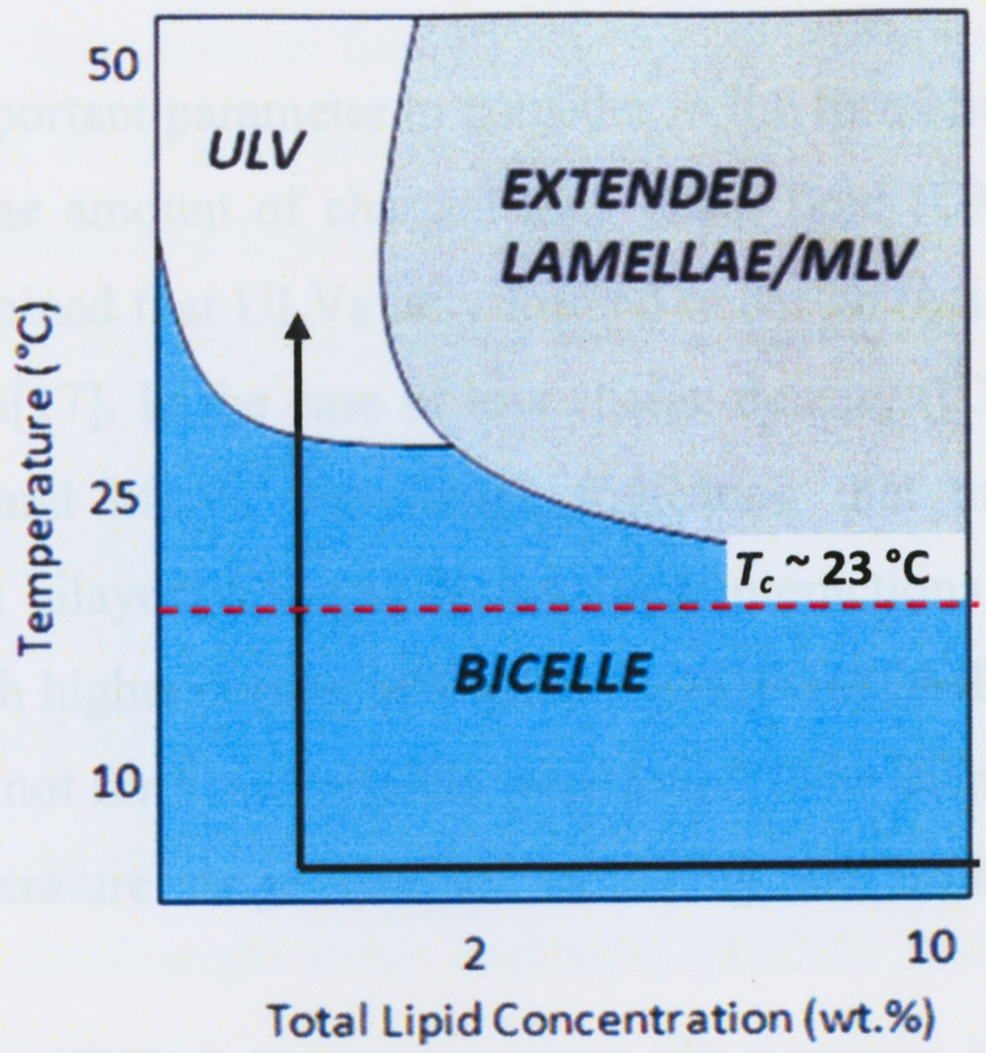

Figure 2.6.1.1. General phase diagram of bicelle, ULV and MLV formation as a function of temperature and total lipid concentration where ULVs are noted to form at low lipid concentrations (< 2 wt.%) and at high temperatures (T > 35°C) (adapted from Katsaras et al., 2005 [41]).

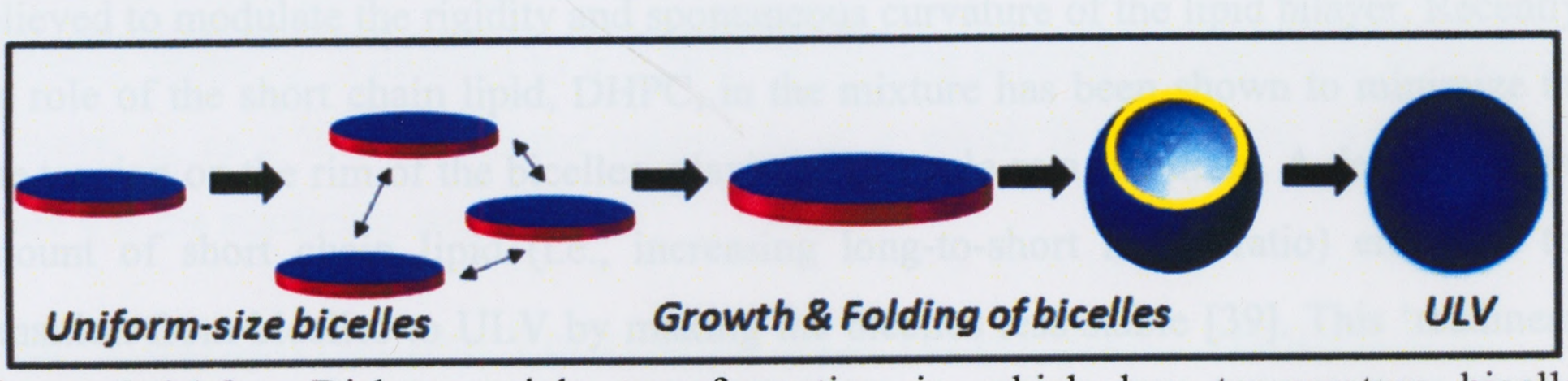

Figure 2.6.1.2. Disk-to-vesicle transformation in which low temperature bicelles coalesce into larger bicelles which then become unstable and fold into vesicles with increasing T ~ 23 °C.

2.6.2 Controlling Parameters of End-State ULV

In addition to the specific pathway in forming ULVs discussed in the previous section, some additional key compositional parameters affect ULV formation. These include charge density, short-to-long chain lipid molar ratio and total lipid concentration, which are further discussed in this section.

2.6.2.1 Charge Density

Charge density is an important parameter to consider in the formation of ULVs. It can be controlled by varying the amount of charged long chain lipid (DMPG) in the mixture. Previously it was determined that ULVs only formed under an optimal charge density of [DMPG]/[DMPC] = 1%[17]. In the case of low charge density ([DMPG]/[DMPC] = 0), coexistence of ULVs and MLVs was found, indicating that there was not enough repulsive force between bilayers, causing face-to-face interactions between neighboring bicelles. In contrast, with higher doping of DMPG (([DMPG]/[DMPC] = 6.7%), at higher temperatures ULVs did not form and bicelles were found to be thermodynamically stable across the entire temperature range studied, indicating too little interaction between neighboring disks [17].

2.6.2.2 Long-to-Short Chain Lipid Molar Ratio

The ratio of the long to short chain (DMPC/DHPC) lipids in the mixture is traditionally believed to modulate the rigidity and spontaneous curvature of the lipid bilayer. Recently, the role of the short chain lipid, DHPC, in the mixture has been shown to minimize the line tension on the rim of the bicelles, playing a key role as a stabilizer. A decrease in the amount of short chain lipid (i.e., increasing long-to-short molar ratio) enhances the transition from bicelles to ULV by making the bicelles less stable [39]. This 'readiness' to fold into vesicles controls the size of the ULVs produced. Previous results indicated that a DMPC/DHPC molar ratios between 2.5 and 4 led to the formation of low-polydispersity ULVs, with vesicle size decreasing with increasing molar ratio of these two phospholipids [39].

2.6.2.3 Total Lipid Concentration

The amount of spacing between discrete particles (in this case bicelles) in solution is controlled by the total lipid concentration (C_{lp}) and can affect the amount of interaction between bicelles in the low temperature regime. This is important for the growth phase of the bicelle system, since a higher concentration can increase the likelihood of collision and coalescing. It is known that two different phase transitions can occur around 23 °C

depending on the C_{lp}: at a high lipid content the bicelle phase transforms into MLVs (C_{lp} > 2 wt.%) while at low lipid content the bicelle phase transforms into ULVs (C_{lp} < 2 wt.%)[12]. Furthermore it is reported that at low lipid concentrations vesicle size decreases slightly with decreasing lipid concentrations, where from 0.5 wt.% to 0.1 wt.% a decrease in average vesicle radius from 134 to 104 Å is seen [39].

2.7 Characterization Of ULVs

2.7.1 Scattering Techniques

ULVs can be characterized using a variety of scattering techniques, including dynamic light scattering (DLS), small-angle x-ray scattering (SAXS) and small-angle neutron scattering (SANS) which provide information about the structure and size distribution of particles in suspension. Each scattering technique follows a similar principle. The wavelength, λ, of radiation (i.e., photon, x-ray, neutron), should match the range of sizes of interest. More specifically, the relationship between the particle radius, R, and the scattering vector, q, is denoted by $q = 2\pi/R$.. Scattering patterns are presented as scattered intensity, I_s, as a function of the magnitude of q which is defined by $(4\pi/\lambda)*\sin(\theta/2)$ where θ is the scattering angle [42, 43]. [15, 42].

2.7.2 Characterization Techniques DLS versus SAXS versus SANS

SANS has several unique features that distinguishes it from both SAXS and DLS.

- The scattering intensity obtained from SANS is not easily contaminated by scattering due to sample container imperfections or dust particles. These problems are difficult to handle with DLS [42].
- DLS provides information on the hydrodynamic radius R_H of particles rather than the true radius [42].
- By varying the ratio of D_2O/H_2O there is a possibility of varying the coherent scattering length density of the solvent with neutron scattering. This makes varying the sample/solution contrast relatively effective and easy to control [42].

- The SAXS technique is difficult to apply to the determination of the structure of some systems where there is a lack of contrast between the solvent and the hydrocarbon portion of the aggregate. X-rays are primarily scattered by the polar part of an amphilphilic molecules making it a more powerful technique for studying the head group region [42, 43]. In addition, X-ray sample transmissions diminish sharply with increased salt concentrations limiting ionic strength dependent studies [43].
- X-ray scattering work involves the risk of irreversible damage to sensitive samples. This requires monitoring of samples for damage, potentially limiting multiple measurements of a sample over time as is used in the case of time-resolved studies [43].

2.7.3 Small-Angle Neutron Scattering

The use of neutrons as a scattering probe began over 60 years ago. Today it is used in a variety of research areas; examples including aspects of magnetism and superconductivity, amorphous materials, polymer conformation and rheology and surfactant and self-assembling systems. Due to the uncharged nature of the neutron it is capable of penetrating deep into materials making it possible in our case to obtain the bulk properties of samples, and to investigate buried interfaces and layered structures [44].

2.7.3.1 Scattering Geometry

The basic SANS scattering principle is presented in Figure 2.7.3.1.1 where a beam of neutrons of intensity I_o (neutrons per square centimeter per second) is directed at a flat sample cell containing particles in solution. The nucleus scatters the neutron to point r in a small cone with a solid angle $d\Omega$. The measurement of the scattered neutron intensity I_s at an angle θ is determined using a detector where a portion of the detector dA is under contact [42, 44]. I_s is collected as a function of the scattering vector, q, $(4\pi/\lambda)*\sin(\theta/2)$ where θ is the scattering angle. Reduction and fitting of the resulting SANS data is further discussed in Chapter 3.

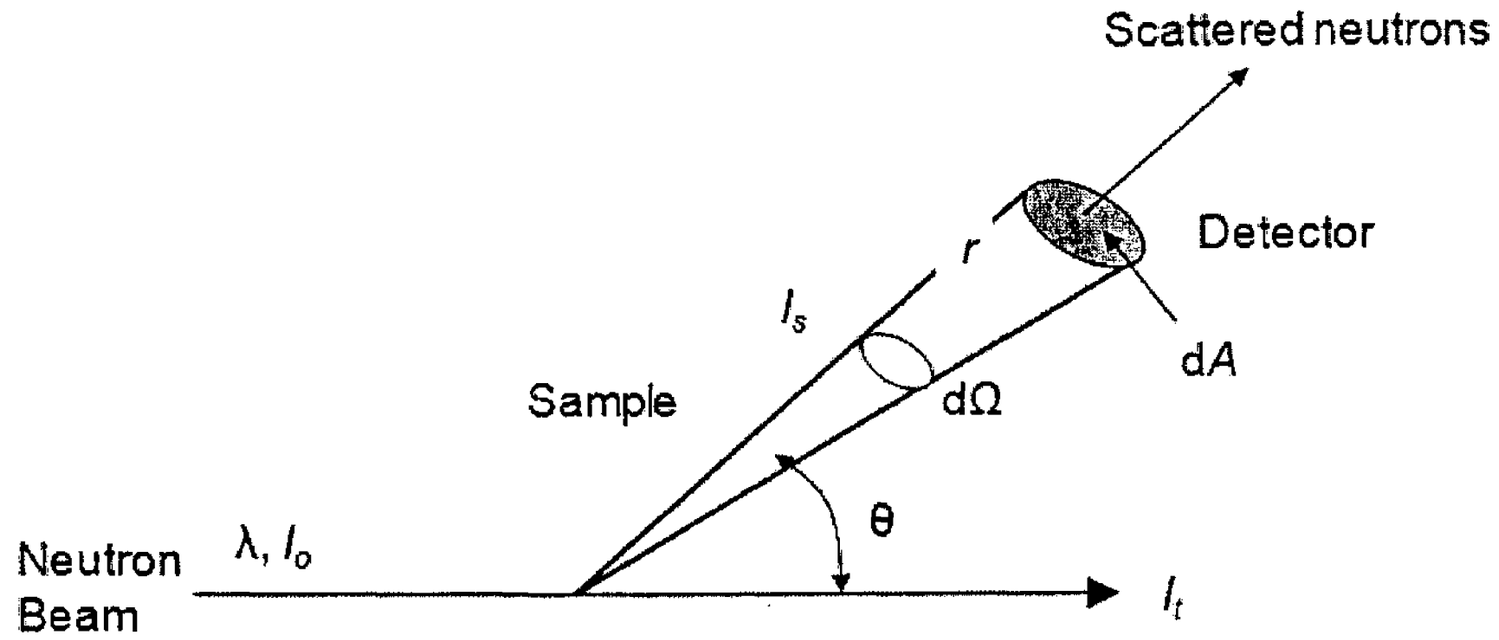

Figure 2.7.3.1.1. Scattering geometry of a SANS experiment (adapted from Chen, 1986; Willis & Carlile 2009 [42, 44]).

2.7.3.2 Instrument Components

A typical SANS instrument is composed of a neutron source, guide tubes, velocity selector or monochromoter, collimator, beam filters, sample holder and a detector. While numerous configurations and variations exist we will discuss in brief the typical instrument make-up and the role of the above mentioned components. A general diagram is presented in Figure 2.7.3.2.1.

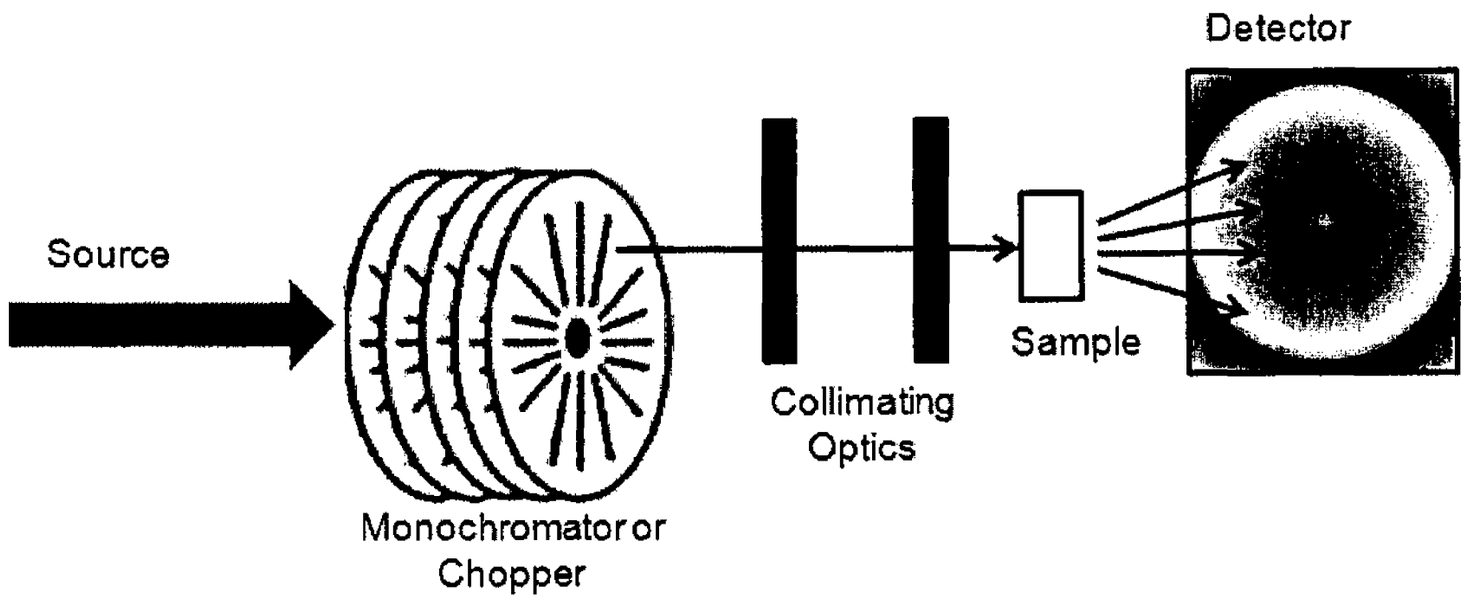

Figure 2.7.3.2.1. Typical instrumental components for a SANS instrument

The neutrons can come from various nuclear reactions; for scattering applications nuclear fission and spallation are considered the most common. Nuclear fission is more common, with the isolation of fissile materials from fuel elements including uranium, thorium or

plutonium. In contrast, the spallation process uses heavy atoms and accelerator-based sources. This nuclear reaction occurs when high-energy particles bombard the nuclei of heavy atoms. Technologically, reactors have approached the maximum neutron fluxes achievable (at best ~10^8 neutrons/cm^2/s) whereas pulsed accelerator sources offer the potential for even higher fluxes [44]. Guide tubes also referred to as guide halls enable the neutron source to be situated away from the experiment in a more spacious region. They are capable of transporting the slow neutron beam without loss of intensity. Furthermore, if the guide tube is slightly curved it is capable of acting as a filter against undesired higher energy neutrons and gamma rays [44].

For the selection of specific neutron energies, velocity selectors (also referred to as mechanical choppers) or single crystal monochromaters are used. Velocity selectors are composed of a cylindrical drum which rotates around its axis where the neutron beam follows a path parallel to the axis of rotation. The drum is fabricated with a neutron absorbing material and has a helical slot cut along its cylindrical surface. Only neutrons with one velocity will pass through the channel without striking either wall of the slot. Changing the speed of the drum changes the neutron energy selected. The second option for selection of specific neutron energies is crystal monochromators. They cause diffraction from a single crystal which provides the simplest method of selecting a monochromatic beam [44, 45].

Collimators can be used to improve instrumental resolution by reducing the angular divergence of the primary or scattered neutron beam. A collimator consists of a series of narrow parallel channels separated by thin absorbing blades; it contains transparent slots and opaque slots which cause the beam to diverge. Ultimately it produces a stack of overlapping beams of narrow divergence; reducing the angular deviation of the overall beam [44, 45].

It is possible to further reduce the signal-to-noise ratio on instruments by interposing filters in the incident or scattered beams. These filters operate by either absorbing unwanted components or by scattering them out of the direct path of the neutron beam. Polycrystalline filters scatter neutrons of given wavelengths; the most common materials are beryllium and graphite. There is a cut off known as the Bragg cut off beyond which

the material becomes transparent to neutrons. This is ideal for the removal of thermal and fast neutrons from an incident beam of cold neutrons [44].

Once the beam is sent through the sample and scattered, detection is required. There exist three types of detectors: gas detectors, scintillation detectors and plate detectors; here we discuss the first two. Gas detectors contain an absorbing gas (i.e., ^{3}He) which causes a nuclear reaction releasing energy causing the reaction products to scatter in opposite directions. The scattered products cause ionization in the gas and this ionization is collected by an anode wire. Alternatively, scintillation detectors use the neutron absorber ^{6}Li in the form of lithium salt which is mixed with the scintillator material, Zinc Sulfide. The burst of light when a neutron is absorbed and ionizing secondary particles are formed is amplified by a photomultiplier. Scintillation counters are in general much better detectors than gas detectors as their detection mechanism is intrinsically 100X faster and does not depend on the drifting of ions [44].

2.7.3.3 Use of SANS to Investigate ULVs

The remainder of this work is focused on investigating self assembling ULVs using the SANS technique. In general, SANS will be used to characterize the ULV and bicelle phase, to investigate ULV size and polydispersity according to varying composition and processing conditions, to investigate the stability of monodisperse ULVs following a high temperature dilution and to quantify low temperature bicelle growth kinetics according to total lipid concentration, ionic strength and temperature ($T < T_c$) and investigate the effects of bicelle growth on the end-state ULVs.

Chapter 3
Materials And Methods

3.1 Materials

The phospholipids, 1,2-dimyristoyl-phosphatidylcholine (DMPC), 1,2-dimyristoyl-phosphatidylglycerol (DMPG) and 1,2-dihexanoyl-phosphatidylcholine (DHPC) were purchased from Avanti Polar Lipids (Alabaster, AL) and were used without further purification. All sample solutions were prepared by dissolving the lipids in deuterium oxide (99.9 % D_2O, Chalk River Laboratories, Chalk River, Canada).

3.2 Sample Preparation

A general preparation procedure was performed as follows for all samples discussed below. A fixed molar ratio of [DMPC]/[DHPC] = 3.3 and varying amounts of DMPG were dissolved to a fixed initial total lipid concentration (C_{lp}) of 10 wt.%. To ensure proper mixing, each sample was vortexed and temperature cycled between 4 and 50 °C a total of 6 times. Consequently, samples were equilibrated at T = 4 °C for 24 hours. All samples were gradually diluted with D_2O in a stepwise fashion to a reduced C_{lp} (i.e., 1 wt.%, 0.3 wt.% or 0.1 wt.%) at 4 °C.

A version of this section has been published in 'Effects of Charge Density and Thermal History on the Morphologies of Spontaneously Formed Unilamellar Vesicles'. Journal of Physical Chemistry B. 2010, 114; 5729 – 5735.

3.2.1 Parameter Optimization and Stability Study

For the investigation of charge density on ULV formation, three different sample solutions were prepared by co-dissolving the lipids to various molar ratios of [DMPG]/[DMPC] (i.e. 0.3 %, 0.8 % and 1.5 %) in D_2O. This study investigated C_{lp} = 0.3 wt. % samples that were slowly annealed at T = 20, 25, 30 and 50 °C for approximately 2 hours per temperature in which SANS experiments were carried out at the end of each 2 hour period. Samples of [DMPG]/[DMPC] ratios of 0.8 % and 1.5 % that were slowly annealed were compared to a second set of 0.3 wt.% samples that underwent a temperature jump, T-jump from 4 °C to 50 °C, and maintained at 50 °C for more than 12 hours. Refer to Figure 3.2.1.1 for the temperature heating profiles and to Table 3.2.1.1 for a summary of experimental conditions discussed.

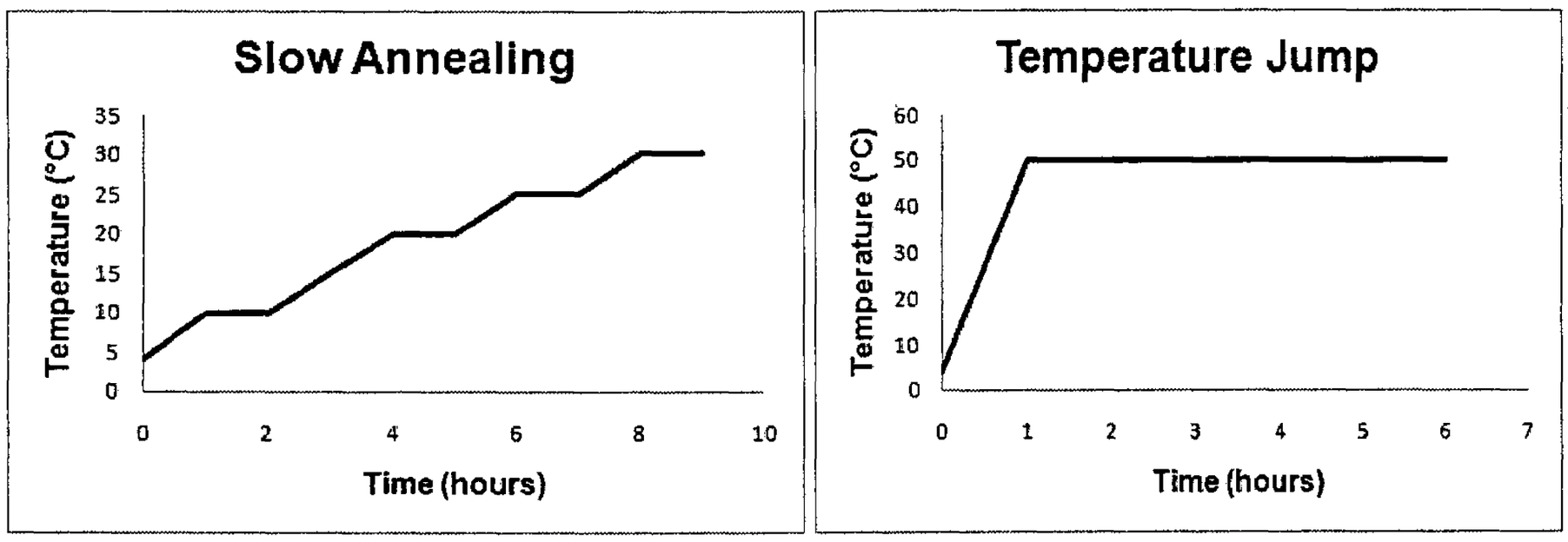

Figure 3.2.1.1. Temperature heating profiles for slow annealing (left) and T-jump (right).

For the investigation of C_{lp} independent ULV stability a second set of 0.3 wt.% and 0.1 wt.% samples were T-jumped from 4 °C to 50 °C, and then kept at 50 °C for more than 12 hours. Finally, some 0.1 wt.% samples were prepared by diluting 0.3 wt.% ([DMPG]/[DMPC] = 0.8% and 1.5%) samples at 50 °C. These samples were used to compare to the same wt.% samples that were diluted at 4 °C and then T-jumped to 50 °C. A set of 0.1 wt.% samples were prepared for ([DMPG]/[DMPC] = 0.8% and 1.5%) via a T-jump to 50 °C using the conventional method described above. These samples were used to compare to the same wt.% samples that were diluted at 50 °C from 0.3 wt.% ([DMPG]/[DMPC] = 0.8% and 1.5%) samples (Table 3.2.1.1).

Table 3.2.1.1. Summary of experimental conditions investigated

Total lipid concentration, C_{lp}	Charge densities [DMPG]/[DMPC]	Thermal pathways
Parameter Optimization		
0.3 wt.%	0.3 %; 0.8%; 1.5%	T-Jump
0.3 wt.%	0.3 %; 0.8%; 1.5%	Slow annealing
Stability Study		
0.3 wt.%	0.8%; 1.5%	T-Jump
0.1 wt.%	0.8%; 1.5%	T-Jump
0.1 wt.%	0.8%; 1.5%	High T dilution

3.2.2 Bicelle Growth Kinetics and ULV Formation

Samples were prepared to a fixed charge density of [DMPG]/[DMPC] = 1% and diluted to C_{lp} = 1 wt.% and 0.3 wt.%. Sodium chloride concentrations, [NaCl] = 0 M and 3 mM were added to both lipid concentrations creating a total of four independent samples. Immediately following preparation, each sample was annealed under constant temperature conditions, T = 10 °C for 24 hours; T = 17 °C and 23°C for 4 hours. SANS data were collected at various time intervals across the total measured times.

ULV formation was investigated following annealing at the fixed low temperature condition by immediately heating samples to 50 °C.

3.3 Vesicle Characterization

3.3.1 Small-Angle Neutron Scattering (SANS)

Preliminary SANS experiments were conducted using N5-SANS located at the Canadian Neutron Beam Centre (CNBC, Chalk River, ON, Canada). Neutron wavelengths (λ) of 5.23, 4.00 and 2.37 Å were used to cover a range of scattering vectors, q, from 0.01 $Å^{-1}$ < q < 0.3 $Å^{-1}$.

SANS experiments for the first study (parameter optimization and stability study) were conducted at the 30 m NG3–SANS [46] located at the NIST (National Institute of

Standards and Technology) Center for Neutron Research (NCNR, Gaithersburg, MD, USA). 6 Å wavelength (λ) neutrons with a $\Delta\lambda/\lambda$ of 11 % were used. Sample-to-detector distances (SDDs) of 1, 5 and 13 m were used, with a detector offset of 20 cm in the case of SDD = 1m. This resulted in a total scattering vector (q) of 0.003 $\text{Å}^{-1} < q < 0.35$ Å^{-1}, [$q = \frac{4\pi}{\lambda}\sin\left(\frac{\theta}{2}\right)$, where θ is the scattering angle].

SANS experiments for the second study (bicelle growth kinetics and ULV formation), were performed using the CG-2 SANS instrument located at Oak Ridge National Lab Neutron Sciences (ORNL, Oak Ridge, TN, USA). Here, an incident neutron beam with a wavelength (λ) of 4.75 Å was used with SDDs of 4 and 18.5 m and a detector offset of 20 cm for a q-range 0.0035 $\text{Å}^{-1} < q < 0.35$ Å^{-1}.

Raw data were corrected for sample transmission, ambient background (blocked beam) and empty cell scattering (also corrected for empty cell transmission). The data were then circularly averaged to yield a 1-dimension scattered intensity profile, which was placed on an absolute scale (cross section per unit volume) using the incident neutron beam flux. Incoherent scattering was obtained from the high q region and subsequently subtracted from the data. These procedures were conducted using a data reduction program (in IGOR-Pro®) developed by NCNR.

3.3.2 Cryogenic-Transmission Electron Microscopy (Cryo-TEM)

Cryo-TEM was used for a direct observation of the ULVs. Sample vitrification was performed using a FEI Vitrobot Mark IV (FEI Worldwide Corp., Oregon, USA) cryo-stage in a controlled environment. A 2 μL sample was placed onto a TEM grid and the excess solution was removed from the grid by blotting with a filter paper. The sample was then vitrified by plunging the grid into liquid ethane and immediately transferred on to the cold sample stage (T = -170 °C) of an FEI Tecnai G2 transmission electron microscope (FEI Worldwide corp., Oregon, USA), which operates at an accelerating voltage of 200 kV in the filtered bright field image mode.

3.4 SANS DATA ANALYSIS

The scattered intensity, $I(q)$ collected as a function of the scattering vector, q can be described by the following relationship:

$$I(q) = \mathrm{n} \langle |F(q)|^2 S(q) \rangle + I_{inc}$$

where n is the number density of particles; $F(q)$ is defined as the form factor; $S(q)$ is the structure factor, describing the arrangement of the objects in solutions; I_{inc} is the incoherent scattering.

Hayter and Penfold described an analytical expression for $S(q)$ by solving the Ornstein-Zernike equation in the mean spherical approximation. This method accounts for the repulsive electrostatic interactions between charged particles and is determined from the total lipid concentration, the dielectric constant of the solvent, the surface charge density of the lipid aggregates, and the ionic strength of solution [47]. When fitting the data from ULV and charged bicelle systems with the addition of [NaCl] this method was employed; however, in very dilute systems $S(q)$ is assumed to be unity and is not considered.

The form factor, $F(q)$ was determined using the core-shell disk model and the polydisperse vesicle model for bicelles and ULVs respectively and are further elaborated below.

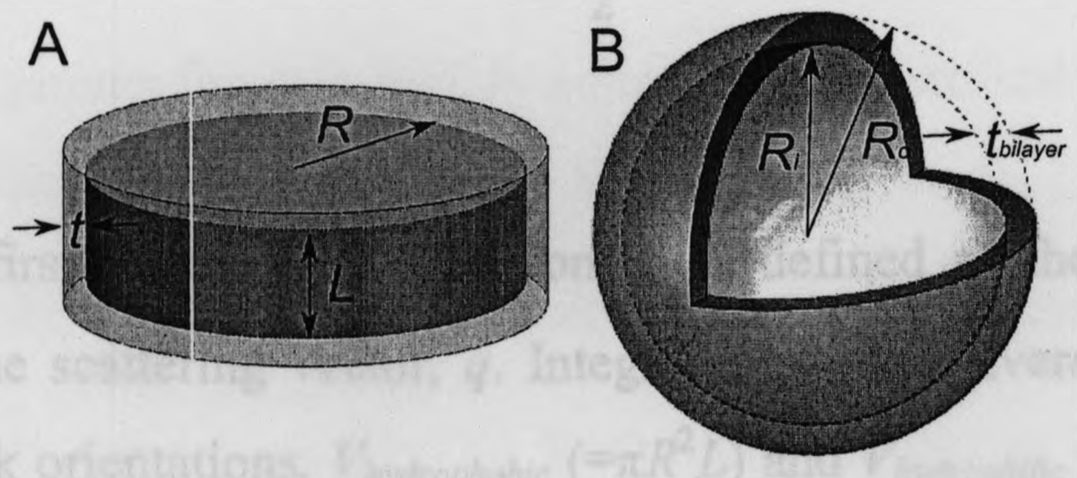

Figure 3.4.1. (A) Bilayered micelles (bicelles) described by the simplified core-shell disk model possessing a hydrophobic core of radius R and thickness L, and a hydrophilic shell of thickness t. (B) ULVs are described by the polydisperse spherical shell model of inner radius R_i, an outer radius R_o, and a polydispersity, p.

3.4.1 Core-Shell Disk Model

This model is used to describe bilayered disks composed of phospholipids in D_2O, where the hydrophilic heads populate the disk's surface forming a shell of uniform thickness *t*. The disk's core is made up of the phospholipid's hydrophobic fatty acid chains, and has a radius *R* and a thickness *L* (Figure 3.4.1A). The core-shell disk model assumes monodisperse bicelles thus reducing the number of fitting parameters, while at the same time adequately describing the SANS data. In the case of a dilute solution, the form factor $P_{disc}(q)$ is proportional to the scattering function $I(q)$ as $\phi_{lipid}P_{disc}(q)$, where ϕ_{lipid} represents the lipid volume fraction. The neutron scattering length densities (SLDs) of the solvent, the disk's core and disk's shell are represented by $\rho_{solvent}$, $\rho_{hydrophobic}$ and $\rho_{hydrophilic}$, respectively, and relate to each other as follows [48, 49]:

$$I(q) = \phi_{lipid} P_{disc}(q) = \int_0^{\pi/2} \frac{f^2(q,\alpha)\sin\alpha d\alpha}{V_{hydrophilic}} \tag{1}$$

where,

$$f(q,\alpha) = 2(\rho_{hydrophobic} - \rho_{hydrophilic})V_{hydrophobic} \frac{\sin(q\frac{L}{2}\cos\alpha)}{(q\frac{L}{2}\cos\alpha)} \frac{J_1(qR\sin\alpha)}{(qR\sin\alpha)}$$

$$+2(\rho_{hydrophilic} - \rho_{solvent})V_{hydrophilic} \frac{\sin[q(\frac{L}{2}+t)\cos\alpha]}{[q(\frac{L}{2}+t)\cos\alpha]} \frac{J_1[q(R+t)\sin\alpha]}{[q(R+t)\sin\alpha]}$$

where $J_1(x)$ is the first order Bessel function; α is defined as the angle between the cylinder axis and the scattering vector, *q*. Integrating over α averages the form factor over all possible disk orientations. $V_{hydrophobic}$ ($=\pi R^2 L$) and $V_{hydrophilic}$ [$=\pi(R+t)^2(L+2t)$] are the volume of the hydrophobic core and hydrophilic shell, respectively. In fitting the data SLDs were constrained to the calculated $\rho_{solvent}$ (6.38×10^{-6} Å^{-2}), while values for ρ_{shell} (= 3.3×10^{-6} Å^{-2} due to inclusion of D_2O) and ρ_{core} (= -4.3×10^{-7} Å^{-2}) were fixed at values obtained from the literature [11, 50].

3.4.2 Polydisperse Vesicle Model

For ULVs shown in Figure 3.4.1B the scattering pattern is described using a polydisperse spherical shell model. A uniform SLD, ρ_{lipid} (3.2 x 10^{-7} $Å^{-2}$), was applied to the bilayer shell to reduce the number of fitting parameters, as the SLD of D_2O, $\rho_{solvent}$, is much greater than ρ_{lipid}. The Schulz distribution function, $f(r)$, was used to describe the size distribution of ULVs, with polydispersity p defined as $\sigma/\langle R_o \rangle$, where σ^2 is the variance of R_o and $\langle R_o \rangle$ is the average R_o [51]. The form factor, $P_{vesicle}(q)$, can be expressed as:

$$P_{vesicle}(q) = \int_0^\infty \frac{1}{V_{vesicle}} f(r) A_0^2(q,r) dr \qquad (2)$$

$$A_0(q,r) = \frac{4\pi(\rho_{lipid} - \rho_{solvent})}{q^3}\{\sin[q(r+t)] - q(r+t)\cos[q(r+t)] - \sin(qr) + qr\cos(qr)\}$$

$$f(r) = \frac{(p^{-\frac{2}{p^2}})(\frac{r}{\langle R_i \rangle})^{(1-p^2)/p^2} e^{-\frac{r}{p^2\langle R_i \rangle}}}{\langle R_i \rangle \Gamma(\frac{1}{p^2})},$$

where $\Gamma(1/p^2)$ is the gamma function used to normalize the distribution function, $\langle R_i \rangle$ is the average inner radius of the vesicle (= R_o – bilayer thickness, $t_{bilayer}$) and $V_{vesicle}$ is the total ULV volume [i.e., $\frac{4\pi}{3}(r+t)^3$] at the inner radius = r. The fitting parameters therefore include $\langle R_i \rangle$, p and $t_{bilayer}$ [Eq (2)]. Both fitting models (in IGOR-Pro®) were developed by and available at NCNR [52].

CHAPTER 4
MORPHOLOGICAL CHARACTERIZATION

To first verify the spontaneous formation of vesicles and the existence of the precursor bicelle phase two principal methods were used: small-angle neutron scattering (SANS) and cryogenic transmission electron microscopy (Cryo-TEM).

4.1 SANS CHARACTERIZATION

Preliminary SANS experiments performed using N5-SANS at CNBC were conducted at $T < T_c$ and at $T > T_c$ ($T_c \sim 23$ °C) to confirm the existence of disks and ULVs respectively. Results from these experiments, shown in Figure 4.1.1 confirm the formation of bicelles at $T \sim 10$ °C (blue squares) and ULVs at $T \sim 50$ °C (red circles). Best fits results obtained using the core-shell disk model and the polydisperse vesicle model (black solid line) are presented in Table 4.1.1 where we obtained disk radius of 80 ± 5 Å and a narrow size distribution ULVs with a radius of 75 ± 5 Å, and polydispersity, $p \sim 0.13$.

The data presented for ULVs (red circles) seen in Figure 4.1.1 are typical of small, uniformly sized vesicles. The best fit results provide the following information in terms of the different q regimes; at q less than ~ 0.015 $Å^{-1}$ the average ULV size is obtained; at q greater than ~ 0.015 $Å^{-1}$ (excluding oscillations) the q^{-2} dependence indicates a planar (single shell) structure; in the higher q region, $q > 0.1$ $Å^{-1}$, the q^{-4} dependence corresponds to the interfacial scattering from the lipid bilayer. Furthermore, the broad peak location and number of oscillations ($q \sim 0.045$ $Å^{-1}$) correspond to the ULV size and range of sizes respectively.

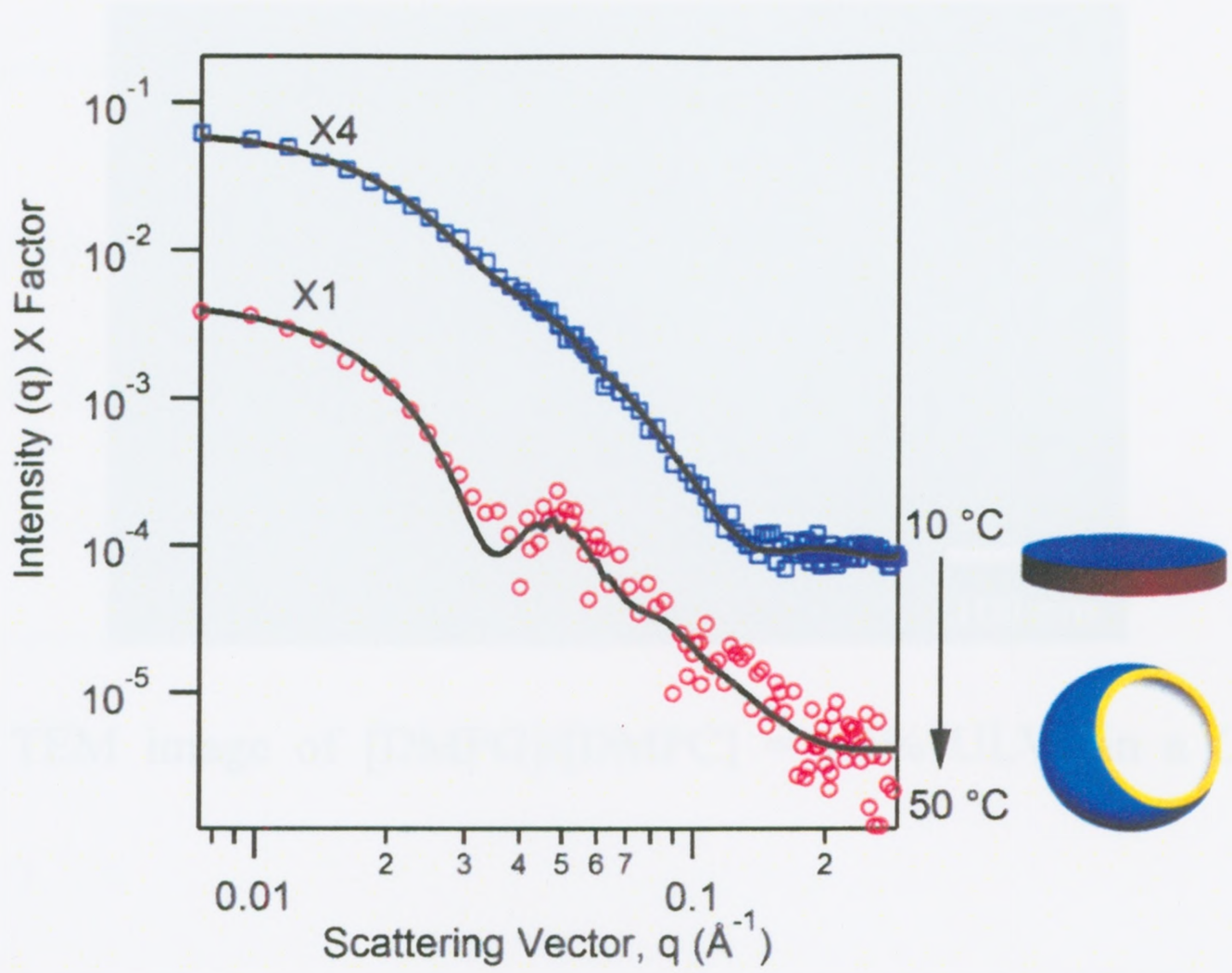

Figure 4.1.1. SANS data and best-fits (solid lines) to the data for C_{lp} = 0.1 wt.% samples at DMPC/DMPH/DMPG = 50/1/15: 10 °C (blue squares) and 50 °C (red circles).

Table 4.1.1. Structural parameters obtained from the best-fits to the data for C_{lp} = 0.3 wt% samples at 10 °C (bicelles) and 50 °C ULVs.

	Radius (Å)	Bilayer Thickness (Å)	Polydispersity
Bicelle	80 ± 5	44 ± 2	--
Vesicle	75 ± 5	30 ± 2	0.13

4.2 Electron Microscopy Characterization

Transmission electron microscopy (TEM) was employed as a means to obtain direct observation of ULVs. Initial experiments were carried out in which the samples were air dried and stained prior to imaging (Figure 4.2.1). This resulted in a collapse of the structure upon drying as can be seen in Figure 4.2.1 where flat, spherical-like shapes with diameters well under 100 nm are present. From this image it is difficult to distinguish between ULV, MLV or bicelle formation. Irrespective, these structures appear to besimilar in size with a narrow size distribution.

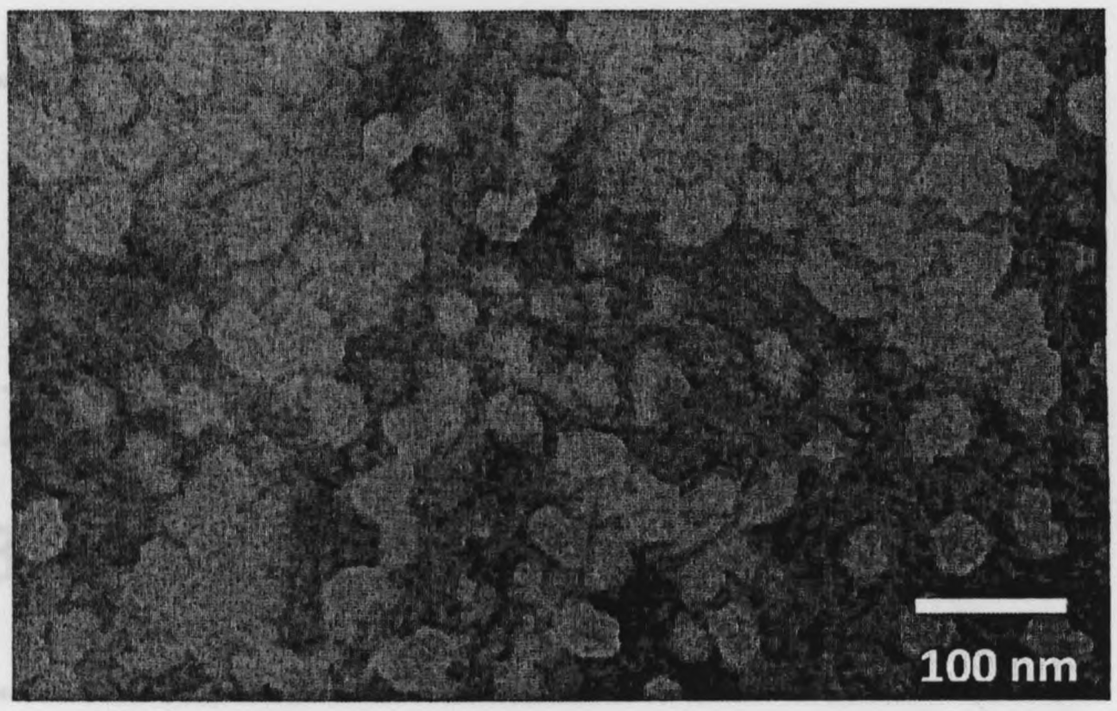

Figure 4.2.1. TEM image of [DMPG]/[DMPC] = 1.5% ULVs in a C_{lp} = 0.3 wt.% solution.

Unlike conventional TEM, the cryogenic-method freezes the ULVs in their liquid suspension instantaneously from the stable 50 °C sample, allowing us to image them in their 3-dimensional morphology. Cryo-TEM was used to obtain an improved visual representation of the ULVs (Figure 4.2.2). These images reveal vesicles with a slightly larger size at a slightly higher lipid concentration (C_{lp} = 0.3 wt.%) than the SANS data presented above (C_{lp} = 0.1 wt.%) where radius, R in this case is approximated at R < 200Å. Furthermore we can see the single lipid bilayer (dark circle) and void interior, verifying the hollow core of the vesicle. This result further confirms the validity of the model used to fit the SANS data at high temperatures.

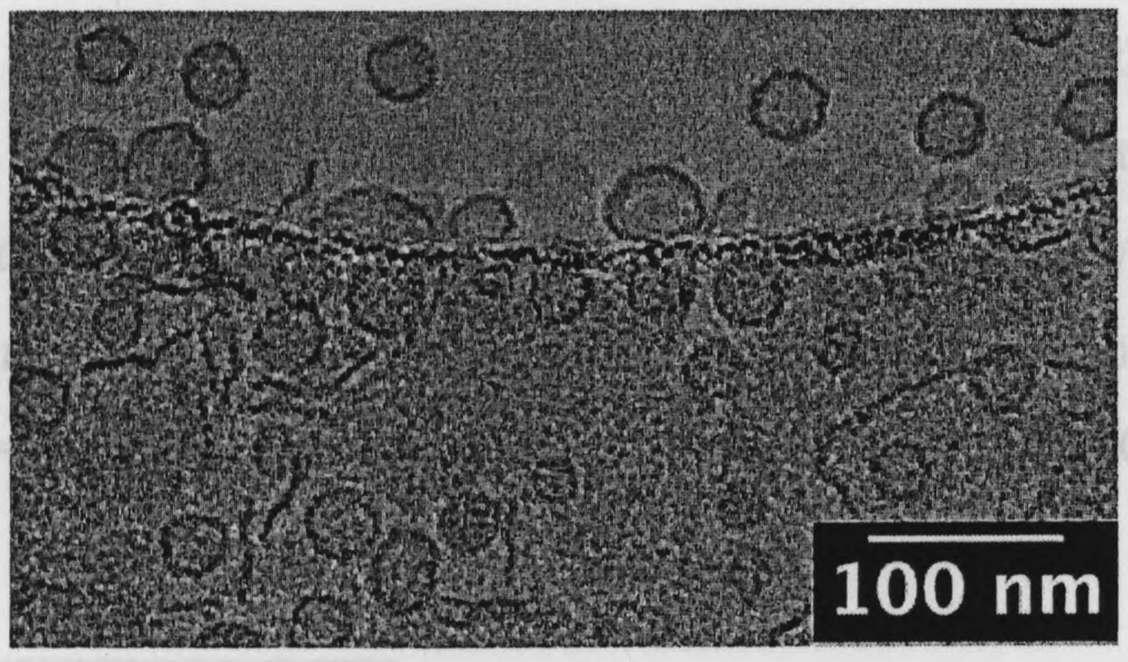

Figure 4.2.2. Cryo-TEM image of [DMPG]/[DMPC] = 1.5% ULVs in a C_{lp} = 0.3 wt.% solution.

CHAPTER 5
PARAMETER OPTIMIZATION AND STABILITY STUDY

5.1 RESULTS

5.1.1 Effect of Charge Density

The effect of charge density on ULV formation was examined by studying ULV size at a number of [DMPG]/[DMPC] ratios (0.3%, 0.8% and 1.5%) and C_{lp} = 0.3 wt.%. Figure 5.1.1.1 shows SANS data of the three samples at T = 50 °C that were slowly annealed from 4 °C. A peak ($q \sim 0.1 Å^{-1}$) associated with the presence of MLVs is observed in the sample with the lowest charge density ([DMPG]/[DMPC] = 0.3), consistent with a previous report on zwitterionic mixtures [14]. For the two other charge density samples, SANS data were best-fit with the polydisperse spherical shell model (solid curves). The best-fit values for $\langle R_i \rangle$ are 770 ± 70 Å and 134 ± 8 Å in the case of [DMPG]/[DMPC] = 0.8% and 1.5%, respectively, indicating that increased charge density yields smaller ULVs (by a factor of ~ 6). To the best of our knowledge, this is the most significant effect on ULV size reported thus far regarding this system. In addition, charge density also seems to affect the size distribution of ULVs. The relative polydispersities of both systems are comparable to each other, while the absolute deviation, σ, in the case of [DMPG]/[DMPC] = 0.8% is three times larger than that of the [DMPG]/[DMPC] = 1.5% sample.

A version of this section has been published in 'Effects of Charge Density and Thermal History on the Morphologies of Spontaneously Formed Unilamellar Vesicles'. Journal of Physical Chemistry B. 2010, 114; 5729 – 5735.

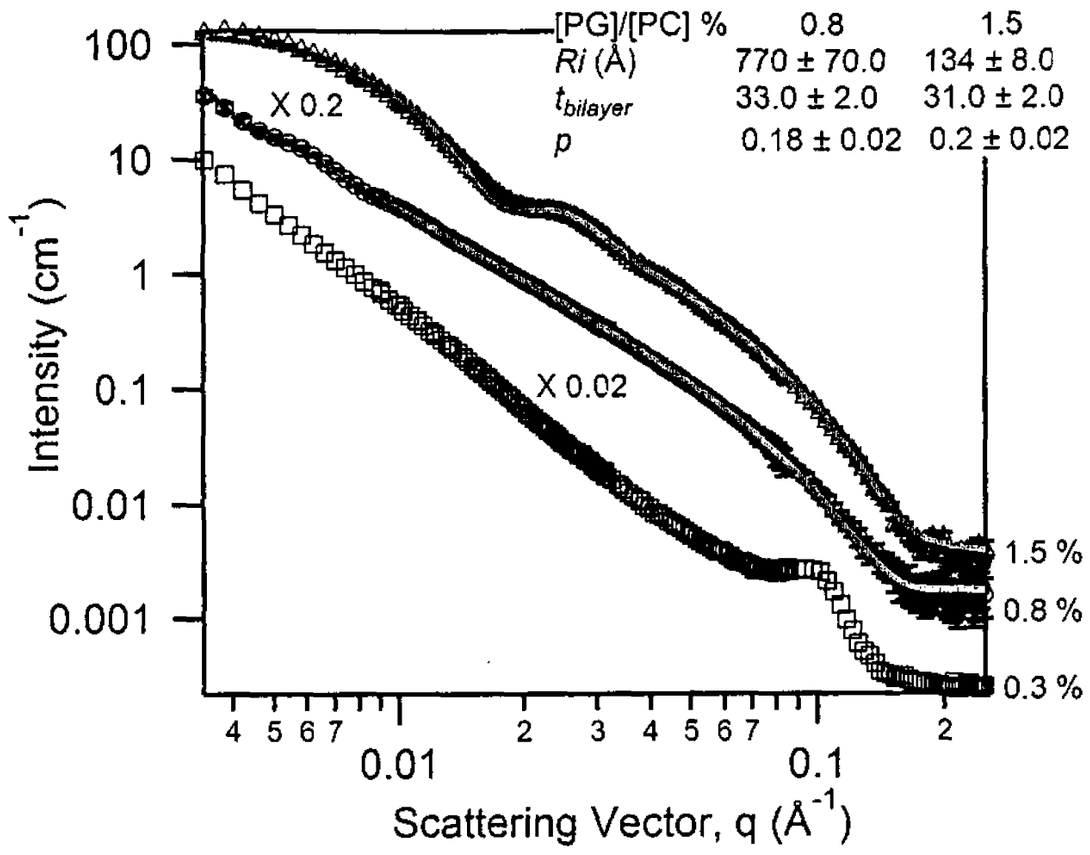

Figure 5.1.1.1. SANS data and best-fits (solid lines) to the data for C_{lp} = 0.3 wt.% samples at T = 50 °C: [DMPG]/[DMPC] = 0.3% (squares), 0.8% (circles), and 1.5% (triangles). For viewing, scaling factors of 0.2 and 0.02 were used for [DMPG]/[DMPC] = 0.8% and 1.5%, respectively. For [DMPG]/[DMPC] = 0.8% and 1.5% data, the best-fits to the data were obtained using the polydisperse spherical shell model. A peak at ~ 0.1Å^{-1}, associated with MLVs, is observed for the [DMPG]/[DMPC] = 0.3% sample.

To study the transition from bicelles to ULVs, SANS experiments were conducted as a function of temperature (20, 25, 30 and 50°C). For the lowest charge [DMPG]/[DMPC] = 0.3% system and C_{lp} = 0.3 wt.%, the solution was visibly opaque indicating the presence of MLVs - also confirmed by the presence of an MLV peak that was present at all temperatures (data not shown). The situation was different, however, in the case of the [DMPG]/[DMPC] = 0.8% and C_{lp} = 0.3 wt.% sample where ULVs formed at low temperature and remained unaltered throughout the range of temperatures studied (data not shown). In the case of the highest charge density sample (i.e., [DMPG]/[DMPC] = 1.5% and C_{lp} = 0.3 wt.%), a clear transition from bicelles to ULVs is observed between 25 and 30 °C (Figure 5.1.1.2). The best-fit structural parameters obtained from the core-shell disk (20 and 25 °C) and polydisperse spherical shell models (30 and 50 °C) are summarized in Table 5.1.1.1. R is found to increase from 266 ± 10 Å to 349 ± 15 Å as T is increased from 20 to 25 °C, in agreement with the notion that prior to forming ULVs, bicelles coalesce as temperature is increased [16]. Between 25 and 30 °C a phase transition takes place, as indicated by the oscillation at $q \sim 0.025$Å^{-1}. Despite this, from

the SANS data we cannot rule out the coexistence of bicelles and ULVs. $\langle R_i \rangle$ of ULV decreases slightly as temperature is increased from 30°C to 50°C, indicating that the ULV structure is unaltered, but that a small amount of lipid (presumably DHPC) dissolves in the aqueous phase. The best-fit shell thicknesses all fall within a reasonable range (~ 32 Å), but slightly smaller than the literature value of ~ 35 Å [53]. Moreover, all the best-fit volume fractions are within 25% of the prepared lipid total concentration, indicating the best-fit models are adequate representations of the morphologies present.

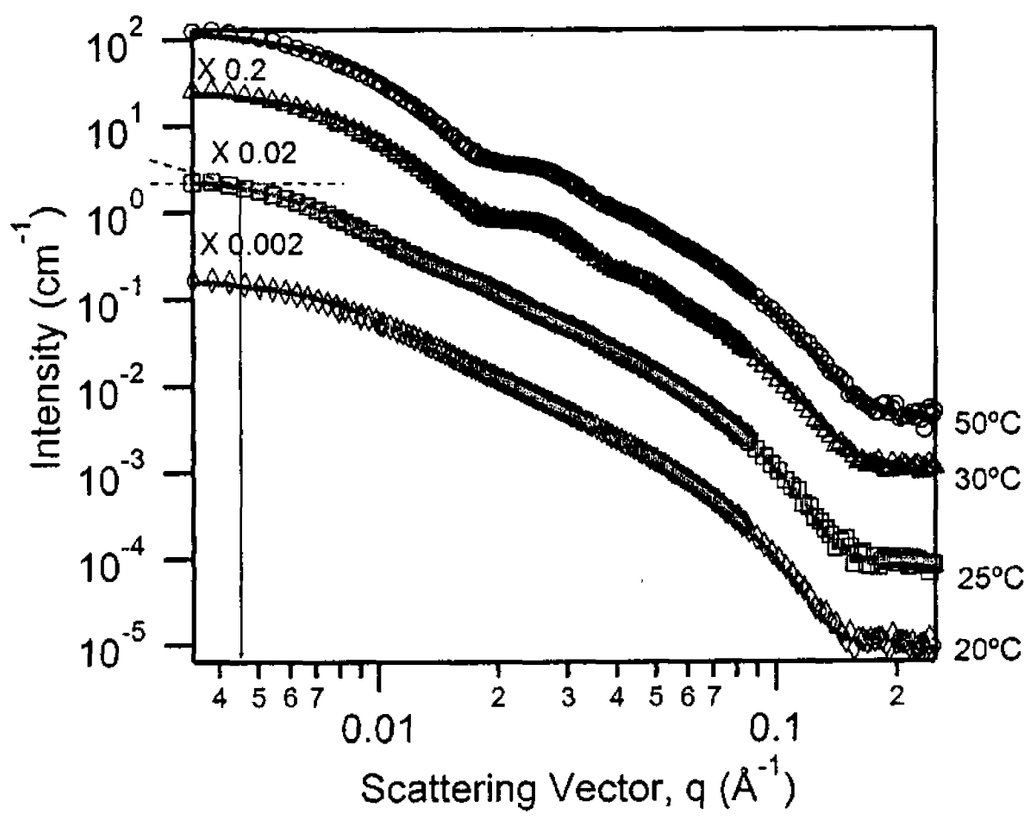

Figure 5.1.1.2. SANS data and best-fits (solid lines) to the data for the [DMPG]/[DMPC] = 1.5% and C_{lp} = 0.3 wt.% sample at various temperatures: T = 20 (diamonds), 25 (squares), 30 (triangles) and 50 (circles) °C. The bicelle–to–ULV phase transition takes place between 25 and 30 °C. Core-shell disk (bicelle) and polydisperse spherical shell (ULV) models were used to fit the data. The dotted lines indicate the two slopes present in the scattering data (25 °C). Their intersection at $q_{intersect}$ ~ 0.0045 Å^{-1} reveals the largest dimension of the aggregates, i.e., the diameter of the bicelles where $\pi / q_{intersect} \sim 2(\langle R \rangle + t)$.

Table 5.1.1.1. Best-fit structural parameters for the [DMPG]/[DMPC] = 1.5% and C_{lp} = 0.3 wt.% sample obtained using the core-shell disk model to fit the low temperature data (T = 20 and 25 °C) and the polydisperse spherical shell model to fit the high temperatures data (T = 30 and 50 °C).

	bicelle				vesicle			
T (°C)	$\langle R \rangle$ (Å)	t (Å)	L (Å)	A_b (Å^2)	$\langle R_i \rangle$ (Å)	$t_{bilayer}$ (Å)	p	A_v (Å^2)
20	266 ± 10.0	10.0 ± 2.0	32.0 ± 4.0	(5.3± 0.6) x 10^5	—	—	—	—
25	349 ± 15.0	9.5 ± 2.0	30.0 ± 4.0	(8.7± 1.0) x 10^5	—	—	—	—
30	—	—	—	—	134 ± 5.0	32.6 ± 3.0	0.21 ± 0.03	(5.8± 0.5) x 10^5
50	—	—	—	—	134 ± 8.0	31.0 ± 3.0	0.22 ± 0.03	(5.8± 0.7) x 10^5

Since almost all of the lipids have the same phosphatidylcholine headgroup, to a first approximation the total surface area of the aggregate morphology is assumed to be proportional to the number of lipids. Therefore a bicelle's surface area, A_b, can be estimated (based on the mid-point of the hydrophilic layer) using the best-fit parameters as follows:

$$A_b = 2\pi (\langle R \rangle + t/2)^2 + 2\pi (\langle R \rangle + t/2)(L+t) \quad (3)$$

A 60% increase in the average surface area of individual bicelles (from 5.3 x 10^5 Å^2 to 8.7 x 10^5 Å^2) with increasing temperature (from 20 to 25 °C) confirms the notion that bicelles grow as a result of increased line tension caused by the loss of DHPC molecules which occupy the bicelle's edge [12]. In the case of ULVs, from the Schulz distribution function, $f(R_i)$, the ULV surface area (both bilayers leaflets) can be determined (Figure 5.1.1.3). The average total ULV surface area, A_v, is thus calculated through the integration of the distribution function (Fig 5.1.1.3). A_v at 30 °C is calculated to be 5.8 x 10^5 Å^2, which is larger than the A_b of bicelle's at 20 °C, and is the result of bicelles coalescing. However the calculated A_v of 30 °C ULVs is ~ 35% less than the A_b of bicelles at 25 °C. Although this result can be partially explained by the loss of DHPC (~23% of the total lipid) from the bicelles into the aqueous phase, we cannot explain the bulk of this difference. At this point we speculate that 25 °C bicelles may contain defects (i.e. perforations), an artifact of bicelle coalescence. However, it should be stressed that bicelle radius is a robust measure as it is model independent (location where the lines that define the two slopes in the data set intersect; *e.g.* ~ 0.0045 Å^{-1} in the case of

[DMPG]/[DMPC]=1.5%; Figure 5.1.1.2). The model is used to determine the morphology and its precise dimensions through the fitting of the entire q range.

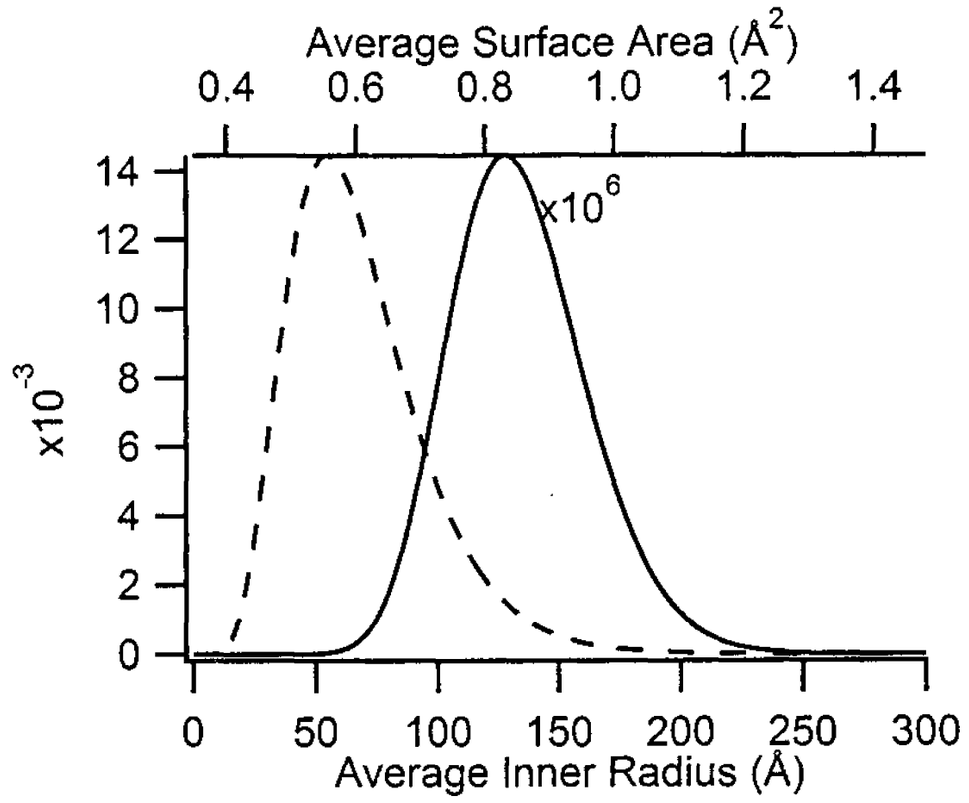

Figure 5.1.1.3. Schulz distribution function for the average inner radius (solid line) and total surface area (dashed line) of the [DMPG]/[DMPC] = 1.5% (C_{lp} = 0.3%) ULVs at T = 30°C.

5.1.2 The Effect of Thermal Path on the Size of ULVs

ULV size distribution was examined as the lipid mixtures underwent two very different thermal path histories, namely a T-jump and slow annealing. Comparison of the SANS data and their corresponding best-fits using the polydisperse spherical shell model is presented in Figure 5.1.2.1. Interestingly, the resultant ULV inner radii in the case of the [DMPG]/[DMPC] = 0.8% sample are very different, i.e. 172 ± 10 Å and 770 ± 70 Å (Table 5.1.3.1) in the case of T-jump and slow annealing processes, respectively. The size variation of ULVs with higher charge density ([DMPG]/[DMPC] = 1.5%) follows the same trend, but is not affected to the same extent, i.e. $\langle R_i \rangle$ is (89 ± 2) Å for T-jump and (134 ± 8 Å) for slow annealing (Table 5.1.3.1). Interestingly, the best-fit volume fractions in both T-jump samples seem to be much less than the prepared lipid concentrations, implying that there could be other types of large aggregates coexisting with ULVs, and which do not contribute to the scattering intensity over the q range examined. Moreover, the shell thickness of the T-jump [DMPG]/[DMPC]=0.8% sample is always best-fit to the lower constraint value of ~25 Å, which is significantly different

from the value in the literature [53], indicating the spherical shell model used is inadequate in describing the entire q range. However, it should be pointed out that the size of ULVs is mainly determined by the oscillation of the SANS data ($q \sim 0.01$ Å^{-1}), thus the value for this morphological feature is robust.

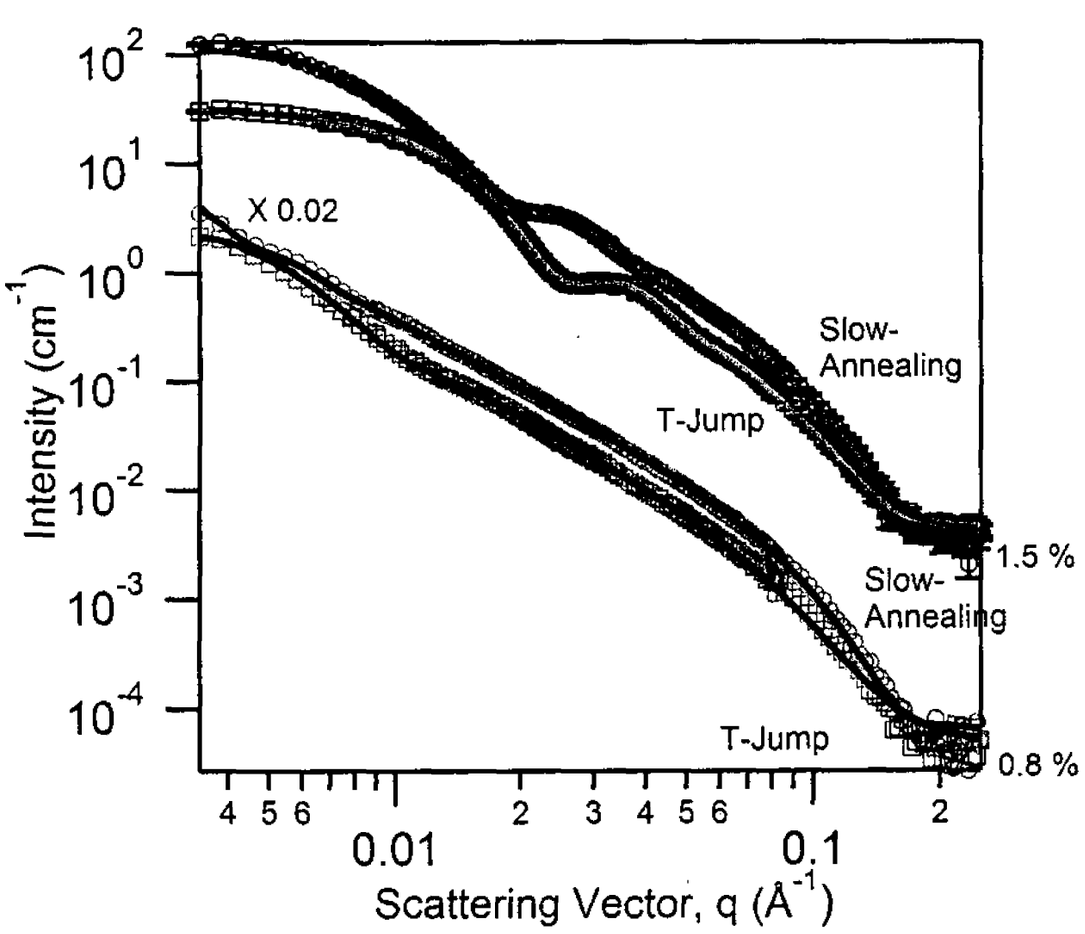

Figure 5.1.2.1. SANS data and best-fits (solid lines) to the data comparing T-jump (squares) and slow annealing (circles) studies for C_{lp} = 0.3 wt.% samples at 50 °C and [DMPG]/[DMPC] = 0.8% (grey) and 1.5% (black). ULVs are found throughout, while their size is larger in the case of the slow annealing process.

5.1.3 Concentration Effect on Size and ULV Stability

ULV stability as a function of total lipid concentration was examined through dilution at high temperature (from C_{lp} = 0.3 wt% to 0.1 wt%), and compared to 0.1 wt% samples diluted at low temperature (i.e. 4 °C) and heated to 50 °C. Figure 5.1.3.1 shows SANS data, and their corresponding best-fits, for C_{lp} = 0.3 wt% and 0.1 wt% samples prepared via a high-T and low-T dilution, respectively. The best-fits to the data are in excellent agreement with each other, indicating that ULVs retain their morphology after high-T dilution for both charge densities. Moreover, low-T dilution clearly causes more polydisperse samples, whereby in the case of the [DMPG]/[DMPC] = 0.8% sample the ULV size could not be determined. The extremely thin shell thickness obtained from the best-fits to the data can be attributed to the same aforementioned reason (i.e., inadequate

model). In the case of [DMPG]/[DMPC] = 1.5%, the size differences between low-T and high-T dilution are insignificant.

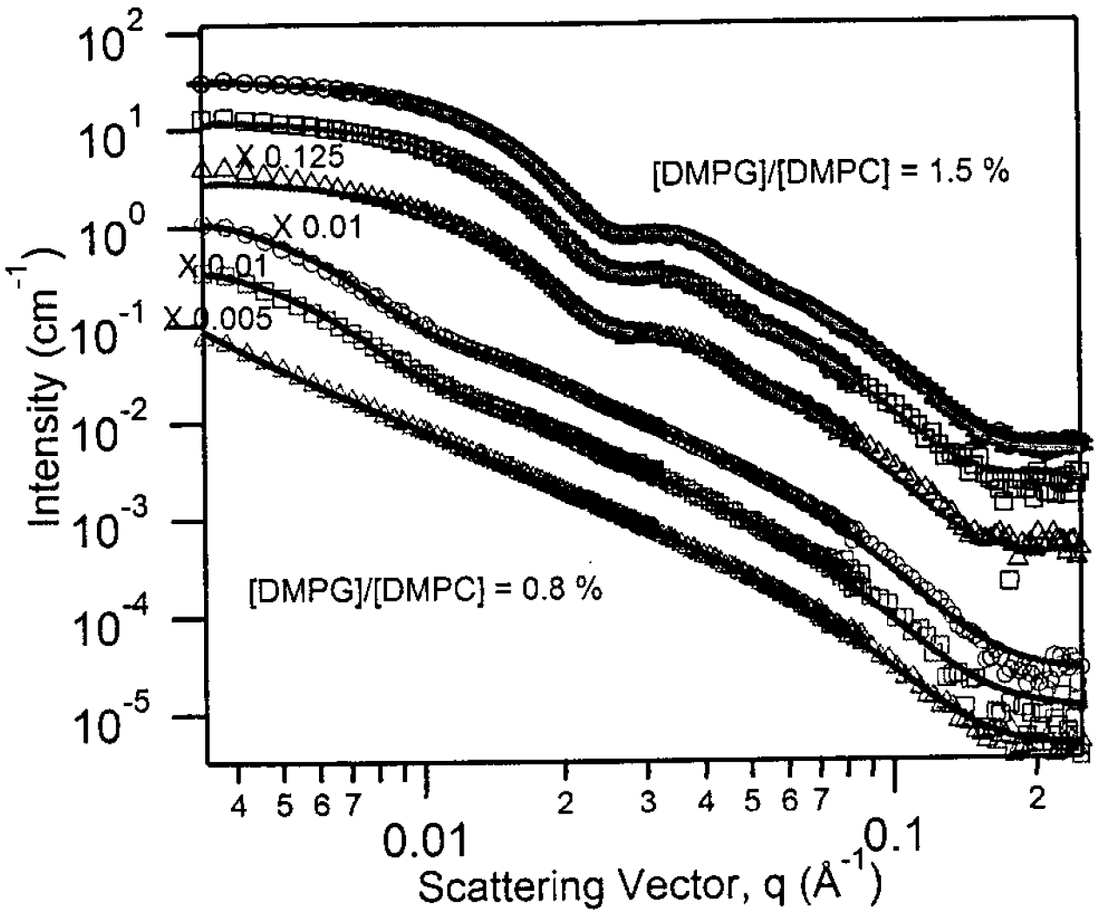

Figure 5.1.3.1. SANS data of [DMPG]/[DMPC] = 0.8% (grey) and 1.5% (black) samples at 50 °C and C_{lp}= 0.3wt% (circles). C_{lp}= 0.1 wt% samples were obtained by either diluting a 0.3 wt% sample at high temperature (squares) or at low temperature (triangles). The ULV morphology was unaffected by high temperature dilution. The solid lines are the best-fits (polydisperse shell sphere model) to the data.

Table 5.1.3.1. Structural parameters obtained from the best-fits to the data for C_{lp} = 0.3 and 0.1 wt% samples diluted at high temperature (HT) and low temperature (LT), respectively.

	[DMPG]/[DMPC] = 0.8 %			[DMPG]/[DMPC] = 1.5 %		
	$\langle R_i \rangle$ (Å)	$t_{bilayer}$ (Å)	p	$\langle R_i \rangle$ (Å)	$t_{bilayer}$ (Å)	p
C_{lp} = 0.3 wt% slow-T	770 ± 70	33.0 ± 2.0	0.18 ± 0.02	134 ± 8.0	31 ± 2.0	0.22 ± 0.02
C_{lp} = 0.3 wt% T-jump	172 ± 10	25.0 ± 0.5	0.40 ± 0.01	89.0 ± 2.0	31. 6 ± 0. 5	0.22 ± 0.02
C_{lp} = 0.1 wt% HT	171 ± 6	25.0 ± 1.0	0.41 ± 0.01	88.0 ± 3.0	30.7 ± 2.0	0.23 ± 0.02
C_{lp} = 0.1 wt% LT	N/A	25.0 ± 2.0	N/A	83.0 ± 5.0	30.0 ± 1.0	0.27 ± 0.01

5.2 DISCUSSION

The three stages of ULV formation reported previously are: (1) The formation of uniform size bicelles; (2) Coalescence of bicelles into large uniform size bicelles; (3) The folding of bicelles into ULVs [12, 15, 16]. Stage (1) is essential in the formation of uniform size ULVs, while stage (2) determines the final size and polydispersity of the ULVs (discussed in detail in this section).

5.2.1 Effect of Charge Density

Earlier studies examining the effect of charge on ULV formation have demonstrated that insufficient or excess charge densities can inhibit their formation, and instead result in the formation of MLVs (insufficient charge) or bicelles (excess charge) [17]. Here we focused on a narrower range of charge densities (i.e. [DMPG]/[DMPC] = 0.3%, 0.8% and 1.5%) in order to gain a more detailed understanding of the system studied, as summarized in Figure 5.2.1.1.

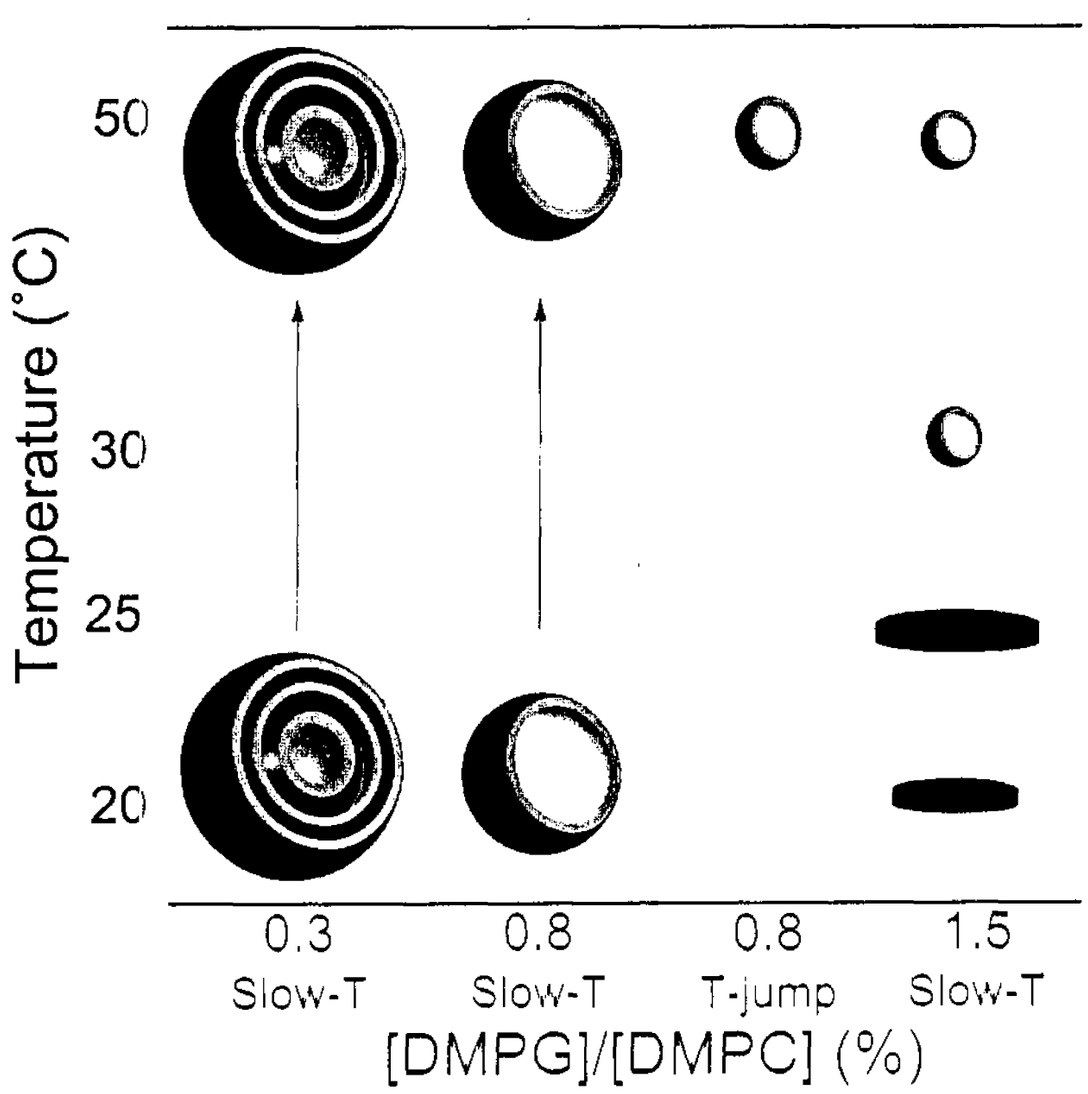

Figure 5.2.1.1. Schematic of the morphologies present in the various DMPG doped C_{lp} = 0.3 wt% systems as a function of temperature. The symbols indicate MLVs (concentric spheres), ULVs (hollow sphere), bicelles (disks).

Low Charge Density: The results of the weakly doped system ([DMPG]/[DMPC] = 0.3 wt%) are similar to those of a neutral system ([DMPG]/[DMPC] = 0), where MLVs were observed [17]. In the case where there is an insufficient amount of charge to cause bilayers to unbind, MLVs are a stable structure [54]. The present system forms an opaque liquid indicative of MLVs for all temperatures studied, a result confirmed by SANS.

Intermediate Charge Density: At a moderate charge density ([DMPG]/[DMPC] = 0.8%) ULVs are observed at all temperatures, indicating that ULVs can form even in the

absence of liquid crystalline DMPC, which undergoes a melting transition temperature at around 23 °C. This result differs from what was previously reported in samples with higher charge densities [12], and can be rationalized as follows: In the case of bicelles being a kinetically trapped morphology (i.e., thermodynamically unstable), collision frequency between bicelles is expected to increase as a function of decreasing charge density (i.e., less Coulombic repulsion). This results in larger size bicelles, which eventually form larger size ULVs. If on the other hand, the bicelles are thermodynamically stable, DMPG may play an important role in retaining the short-chain DHPC within the bicelles, and thus preventing them from growing.

High Charge Density: Increasing charge density ([DMPG]/[DMPC] = 1.5%) results in bicelles appearing at low temperature and ULVs at high temperature. This transition between bicelles and ULVs takes place somewhere between 25 and 30 °C, slightly greater than T_M for DMPC (23 °C). In fact, T_c has been reported to increase with increasing C_{lp} and charge density [14]. The [DMPG]/[DMPC] = 1.5% ULVs are smaller than those of [DMPG]/[DMPC] = 0.8% either because they experience less collisions (i.e. less opportunities to coalesce into larger bicelles) or they are more stable with higher content of DMPG.

5.2.2 Effect of Thermal Path

One of the most interesting findings of the present study is the dramatic difference in ULV size as a function of different thermal annealing (slow annealing vs. T-jump, as shown in Figure 5.1.2.1 and Table 5.1.3.1). The slow annealing process effectively prolongs the coalescing period (stage 2), increasing the probability of bicelle collisions, which eventually results in the formation of larger ULVs. The fact that this effect is not as significant in the case of the higher charge density sample (i.e. [DMPG]/[DMPC] = 1.5%, as shown in Table 5.1.3.1) is most likely the result of strong Coulombic repulsion. Nevertheless, an 80 Å increase in bicellar radius over 5 °C (i.e. from 20 °C to 25 °C) in approximately 2 hours still supports the notion of bicelles growing through collisions with one another, even at higher charge densities. Interestingly, for the intermediate charged [DMPG]/[DMPC] = 0.8% (0.3 wt%) sample, large ULVs are found at low temperatures, while the same sample experiencing a T-jump yields much smaller ULVs.

This observation implies that for this system stage 2 takes place at low temperatures - on the order of minutes, compared to seconds for the T-jump and the hours that it takes to collect good SANS data.

5.2.3 Effect of C_{lp} and Stability of ULVs

The size invariance of the current spontaneously formed ULVs as a function of C_{lp} and thermal annealing protocol is a distinct advantage over other surfactant systems [13, 14], where ULV size depends on C_{lp} [11, 19]. In fact, this can be explained by the proposed mechanism of ULV formation [12, 16]. The size of low temperature bicelles has been reported to be weakly dependent on C_{lp} [11, 17]. If we assume that the collision frequency of aggregates in the case of higher C_{lp} samples is greater than that of lower C_{lp} samples, it then follows that larger ULVs are expected to form in the case of high C_{lp} samples. The present SANS data only show small differences in the size of ULVs between C_{lp} = 0.3 and 0.1 wt.% samples, probably due to the already low frequency of bicelle coalescence in C_{lp} = 0.3 wt.% samples. However, ULV size should not change if the system is diluted at or after stage 3, where ULVs are the stable morphology. The invariance of ULV size seen here for high and intermediate charge density samples undergoing high temperature dilution is consistent with the proposed mechanism, implying that ULVs are stable.

CHAPTER 6
BICELLE GROWTH KINETICS AND END-STATE ULV PROPERTIES

6.1 RESULTS

The hypothesis of disk interaction, coalescence and growth was confirmed by our previous results (Chapter 5) where an increase in disk size (R_v ~ 266 to 349 Å) with increasing temperature from 20 °C to 25 °C over 2 hours was resolved using SANS. These results also indicated that the increase in disk size is quantifiable on a reasonable time scale. To gain more insight into the low temperature bicelle phase we conducted a study on the growth of disks and on its role in the end-state vesicle properties. Of specific interest is disk growth as a function of three key parameters; temperature, total lipid concentration and ionic strength. Our experiments conducted at Oak Ridge National Lab (ORNL) offer the unique possibility for time-resolved studies due to their high neutron flux and the large q-range covered in a single instrumental setting ($0.0032 < q < 0.07$ Å^{-1}).

6.1.1 Bicelle Growth

The effects of temperature, total lipid concentration and ionic strength on the growth of disks over time were investigated using CG-2 SANS at ORNL. We examined the time dependent growth at three temperatures, T = 10, 17 and 23 °C; at varying total lipid concentrations, C_{lp} = 0.3 and 1 wt.% and varying ionic strengths, [NaCl] = 0 and 3mM. The matrix of experimental conditions used is summarized in Table 6.1.1.1. Resulting SANS data and their corresponding best fit curves are presented in Figure 6.1.1.1. Each block represents a combination of C_{lp} and [NaCl]: (a) C_{lp} = 1 wt.%, [NaCl] = 0mM; (b) C_{lp} = 1 wt.%, [NaCl] = 3mM; (c) C_{lp} = 0.3 wt.%, [NaCl] = 0mM; (d) C_{lp} = 0.3 wt.%.

[NaCl] = 3mM and each set of curves represents data collected across different time intervals at 10 °C for ~24hrs (grey), 17 °C for ~ 4hrs (blue), 23 °C for ~ 4hrs (purple). In general, as time increases we observe two possible changes in the SANS curves; an increase in intensity, I (which cannot seen in the figures due to multiplication by an arbitrary factor) and a shift in the bend position with respect to the scattering vector, q. The change in bend position is denoted by an arrow through the data at 17 °C (blue) in Figure 6.1.1.1a. These variations in the curve indicate a change in the average disk size which is resolved by fitting the data with the core-shell disk model (solid lines in Figure 6.1.1.1). When fitting with this model we make two major assumptions: (1) at any given time disks are monodisperse, therefore disk growth is uniform and (2) that bicelle growth favors coalescing on the disks' edges, thus flat cylindrical geometries are maintained (refer to Figure 6.1.1.2).

Table 6.1.1.1. Summary of experimental conditions for all samples

Temperature (°C)	Lipid content (wt. %); Ionic strength (mM)			
10	0.3 wt.%; 0 mM	0.3 wt.%; 3 mM	1 wt.%; 0 mM	1 wt.%; 3 mM
17	0.3 wt.%; 0 mM	0.3 wt.%; 3 mM	1 wt.%; 0 mM	1 wt.%; 3 mM
23	0.3 wt.%; 0 mM	0.3 wt.%; 3 mM	1 wt.%; 0 mM	1 wt.%; 3 mM

As the results in Figure 6.1.1.2 indicate, we observe growth at all temperatures for all samples. As shown in Figure 6.1.1.2c, at [NaCl] = 0mM; C_{lp} = 0.3 wt.% we see an increase in average disk radius from 131.0 ± 4 Å to 169.0 ± 5 Å over 24 hours at 10 °C. For the same sample at 23 °C (Figures 6.1.1.2a) we see a much greater increase in average disk radius from 172.4 ± 5 Å to 280.0 ± 10 Å over a much shorter time period (~4hrs), demonstrating the effect of temperature on the growth of disks. If we take a closer look at Figure 6.1.1.1b and 6.1.1.1d we see that for both 23 °C at t_{final}, the curve begins to change with an irregular oscillation in the high q-range ($q > 0.05 Å^{-1}$), which we hypothesize to be an initial transition of disks into ULVs, making it difficult to fit with the core-shell disk model since the disk may no longer be an open ramified structure. As a result, the curve for t_{final} at 23 °C in Figure 6.1.1.1d has not been fitted. Furthermore, we

find that both total lipid concentration and ionic strength significantly impact the rate of growth, which is further discussed below.

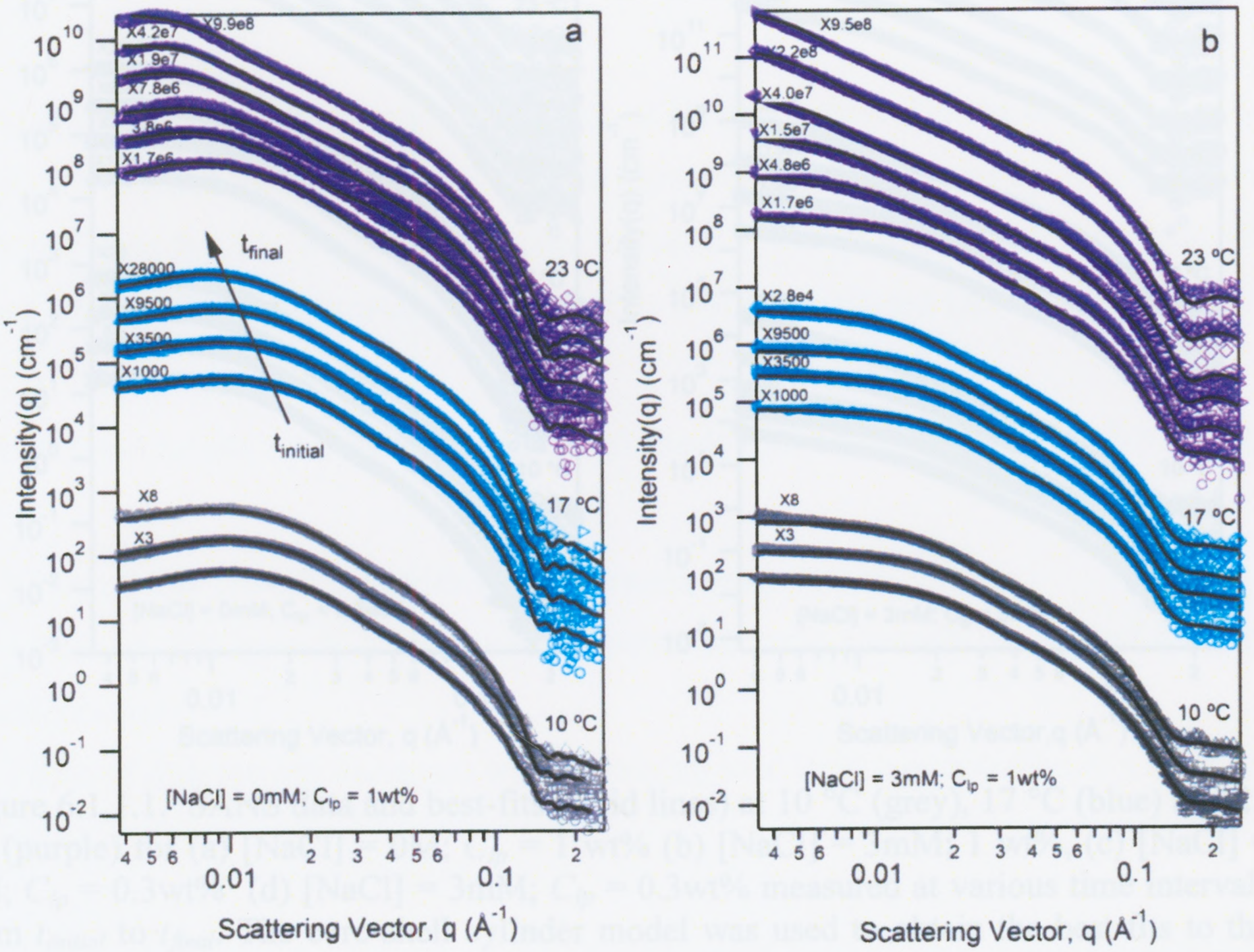

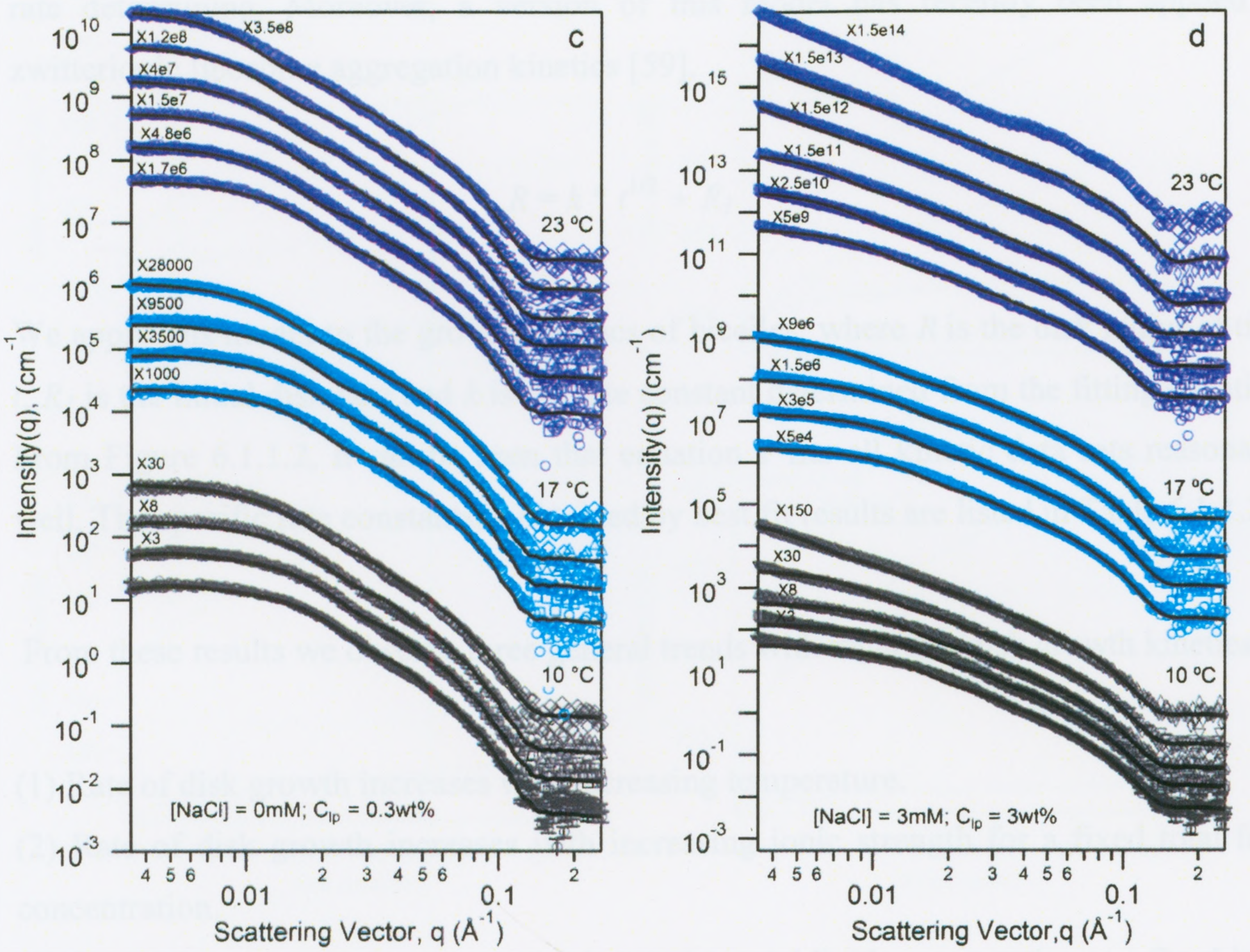

Figure 6.1.1.1. SANS data and best-fits (solid lines) at 10 °C (grey), 17 °C (blue) and 23 °C (purple) for (a) [NaCl] = 0M; C_{lp} = 1 wt% (b) [NaCl] = 3mM; 1 wt%, (c) [NaCl] = 0M; C_{lp} = 0.3wt% (d) [NaCl] = 3mM; C_{lp} = 0.3wt% measured at various time intervals from $t_{initial}$ to t_{final}. The core-shell cylinder model was used to obtain the best fits to the data. A slight change in the curve is seen as time increases, associated with the growth of the disks.

The disk radius, *R*, is plotted as a function of time in Figure 6.1.1.2. It can be seen that under all experimental conditions used, disk size increases over time at different rates. Moreover, the growth rate and ultimate disk size are not only a function of temperature but also of ionic strength and total lipid concentration.

To gain a better understanding of the data, the results are fitted with a power-law model between disk radius and time (Equation 1). This model has been used to interpret growth occurring during oxidation processes and colloid aggregation processes [55-58]. When applied to colloid aggregation this model assumes the diffusion of colloidal particles is

rate determining. Moreover, a version of this model has recently been applied to zwitterionic liposome aggregation kinetics [59].

$$R = k * t^{1/2} + R_1 \quad (1)$$

We apply this model to the growth kinetics of bicelles, where R is the disk radius at time t, R_1 is the initial disk size and k is the rate constant determined from the fitting equation. From Figure 6.1.1.2, it can be seen that equation 1 fits all kinetic data sets reasonably well. The specific rate constants, k obtained by best fit results are listed in Table 6.1.1.2.

From these results we observe three general trends with regard to disk growth kinetics:

(1) Rate of disk growth increases with increasing temperature.
(2) Rate of disk growth increases with increasing ionic strength for a fixed total lipid concentration.
(3) Rate of disk growth decreases with increasing total lipid concentration at a fixed ionic strength.

The fastest disk growth rate is observed at the highest annealing temperature (23 °C), lowest total lipid concentration (C_{lp} = 0.3 wt.%) and highest ionic strength ([NaCl] = 3mM) investigated, with $k \sim 1.40 \times 10^5$ Å^2/hr. In contrast, the slowest disk growth rate is observed at the lowest temperature (10 °C), highest total lipid concentration (C_{lp} = 1 wt.%) and lowest ionic strength ([NaCl] = 0mM) investigated, with k ~ 4.80 Å^2/hr – a difference of over 29 000 fold in the amount of interaction and growth between the two samples.

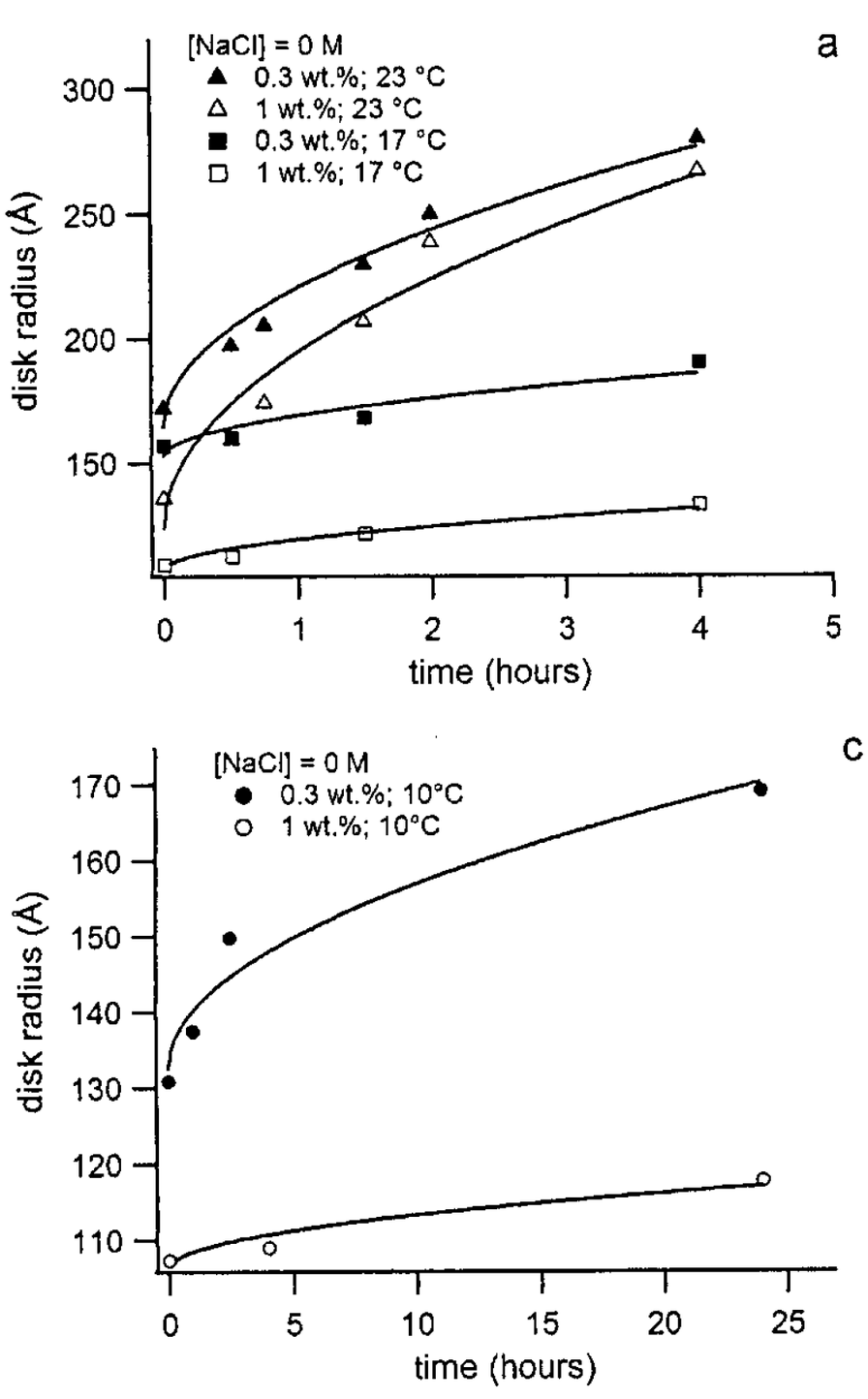

Figure 6.1.1.2. Average disk radius as a function of time for all samples. All data sets are fit with a power-law to obtain the kinetic constant, *k*.

Table 6.1.1.2. Kinetic constants, k_x (Å^2/hr) obtained from the power-law model for all samples at 10, 17 and 23 °C where *x* represents the annealing temperature.

[NaCl]; C_{lp}	k_{10}	k_{17}	k_{23}
0 mM; 1 wt%	4.80×10^0	1.49×10^2	5.05×10^3
3 mM; 1wt%	1.91×10^1	4.87×10^2	4.49×10^4
0 mM; 0.3 wt%	5.98×10^1	2.75×10^2	3.19×10^4
3 mM; 0.3 wt%	5.52×10^3	2.26×10^3	1.40×10^5

6.1.2 End-State Vesicle

All samples which underwent slow annealing at 10, 17 and 23 °C were subsequently heated to 50 °C to determine the effect of annealing on the end-state ULVs where SANS experiments were conducted at 50 °C. All resulting curves and their corresponding best fits are presented in Figure 6.1.2.1 where each block represents a different combination of C_{lp} and [NaCl] (a) C_{lp} = 1 wt.%, [NaCl] = 0mM; (b) C_{lp} = 1 wt.%, [NaCl] = 3mM; (c) C_{lp} = 0.3 wt.%, [NaCl] = 0mM; (d) C_{lp} = 0.3 wt.%, [NaCl] = 3mM and each curve within each block represents a different annealing temperature, 10 °C annealing (orange); 17 °C annealing (green); 23 °C annealing (blue). From looking at the SANS data a general trend is observed where there is a shift in the peak position towards the lower q range and an increase in peak broadness (width of the peak) with increasing annealing temperature. The relative change is closely related to the average vesicle radius, R_v and polydispersity, p which were determined using the polydisperse spherical shell model and are summarized in Figures 6.1.2.2a and Figure 6.1.2.2b respectively as a function of annealing temperature.

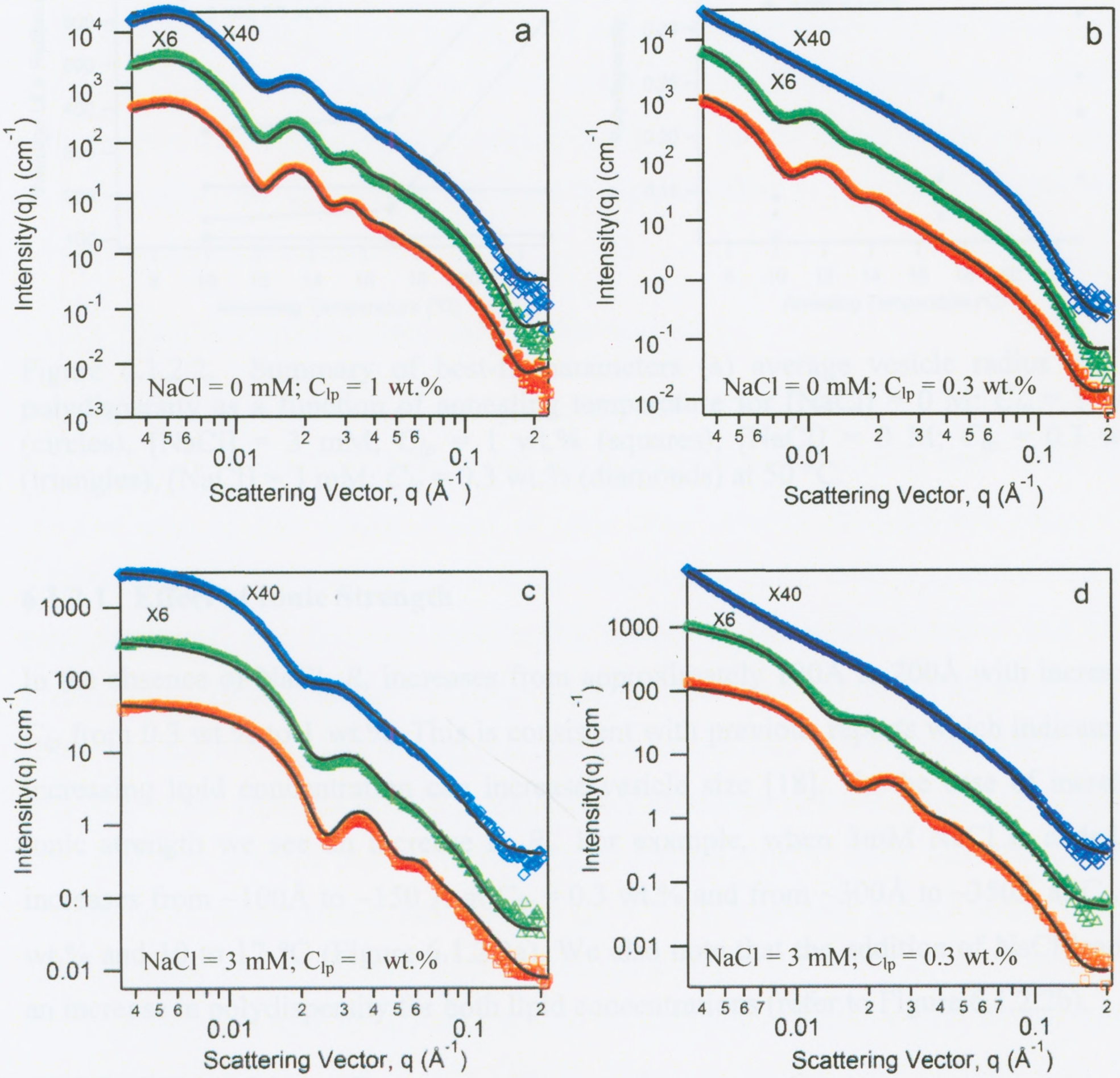

Figure 6.1.2.1. SANS data and best-fits (solid lines) for all samples (indicated in bottom left) at 50 °C following various annealing temperatures - 10 – 50 °C (orange), 17 – 50 °C (green), 23 – 50 °C (blue).

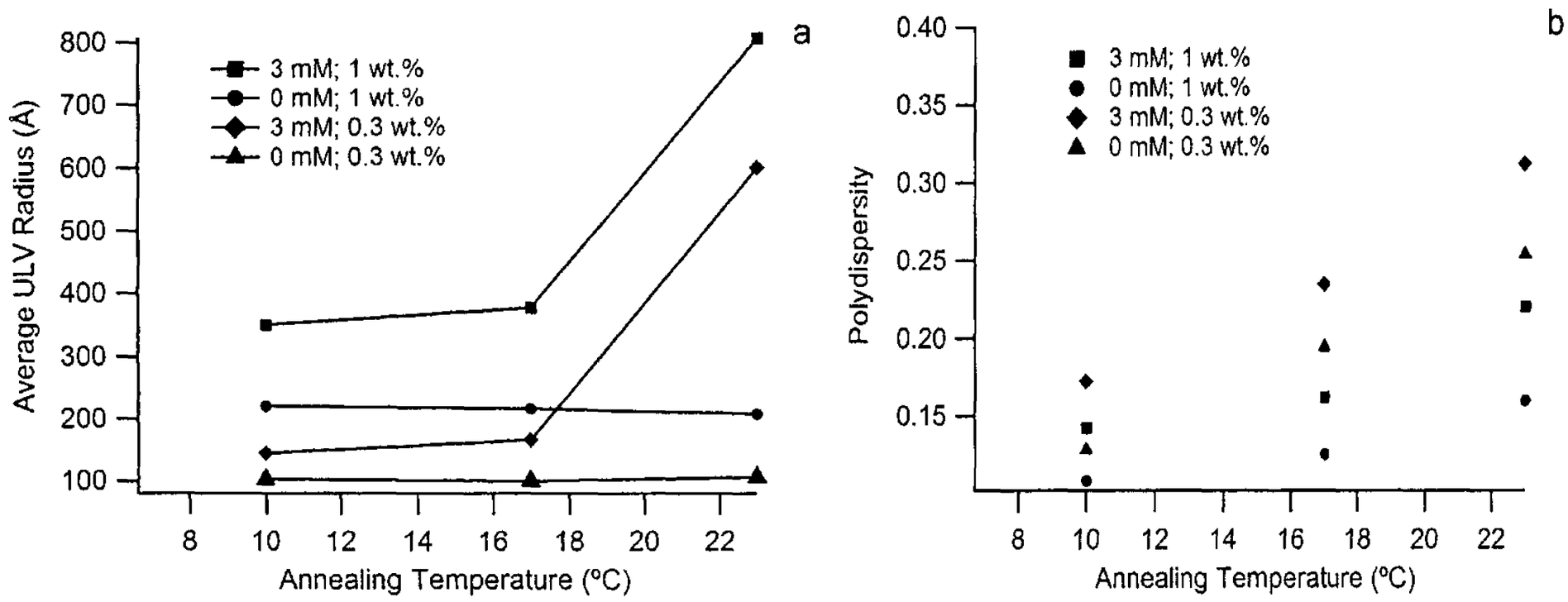

Figure 6.1.2.2. Summary of best-fit parameters (a) average vesicle radius and (b) polydispersity as a function of annealing temperature for [NaCl] = 0 M; C_{lp} = 1 wt.% (circles), [NaCl] = 3 mM; C_{lp} = 1 wt.% (squares), [NaCl] = 0 M; C_{lp} = 0.3 wt.% (triangles), [NaCl] = 3 mM; C_{lp} = 0.3 wt.% (diamonds) at 50 °C.

6.1.2.1 Effect of Ionic Strength

In the absence of NaCl, R_v increases from approximately 100Å to 200Å with increasing C_{lp} from 0.3 wt.% to 1 wt.%. This is consistent with previous reports which indicate that increasing lipid concentration can increase vesicle size [18]. In the case of increased ionic strength we see an increase in R_v. For example, when 3mM NaCl is added, R_v increases from ~100Å to ~150 Å at C_{lp} = 0.3 wt.% and from ~300Å to ~350Å at C_{lp} = 1 wt.% and 10 to 17 °C (Figure 6.1.2.2a). We also note that the addition of NaCl leads to an increase in polydispersity for both lipid concentrations (refer to Figure 6.1.2.2b).

6.1.2.2 Effect of Annealing

When comparing the effects of annealing on both C_{lp} = 0.3 wt.% and 1 wt.% samples (in the absence of NaCl), R_v tends to remain constant however, a gradual increase in p as annealing temperature increases is observed (Figure 6.1.2.2b). We see the most significant effect of this with [NaCl] = 3mM and C_{lp} = 0.3 wt.% where polydispersity varies from 0.17, 0.24 to 0.31 when samples were annealed at 10 °C, 17°C and 23 °C respectively. In contrast, annealing temperature in the presence of NaCl has an overall effect on both the average vesicle size, R_v and the polydispersity, p where both increase gradually as annealing temperature increases. This is different from the case with no

NaCl where no change in R_v was seen with annealing temperature. The most significant effect occurs at 23 °C where there is a significant increase in size and polydispersity, where $R_v > 600$ Å and $p > 0.21$ for $C_{lp} = 0.3$ and 1 wt.% samples compared to the T-jump sample at $C_{lp} = 1$ wt.% with $R_v \sim 300$ Å and $p \sim 0.15$. These results are in agreement with our previous results where annealing rate had a greater effect on the lower charge density sample; the addition of NaCl has a similar effect in reducing repulsive forces between particles (Chapter 5).

6.1.2.3 Role of Precursor Disk in ULV Formation

From the best-fit parameters of disk radius, R_d, and shell thickness, $t_{bilayer}$ (obtained from fitting with the core-shell disk model) the average absolute surface area of the disks (surface area of two planar faces) at each time interval is calculated ($A_{disk} = 2\pi (\langle R_d \rangle + t_{bilayer}/2)^2$). We compare the average surface area of the disk, A_{disk} at the final time point measured, t_{final} for each independent sample to the average surface area of the vesicle, $A_{vesicle}$ (where $A_{vesicle} = 4\pi [\langle R_o \rangle^2 + \langle R_i \rangle^2]$) to compare the role of the annealed disk in the end-state ULV. The average disk surface area at t_{final} and average vesicle surface area determined from the best fit parameters are presented in Table 6.1.2.1. Of interest is that slow annealing of $C_{lp} = 1$wt.% samples formed smaller disks than the 0.3 wt.% samples at all temperatures, however the $C_{lp} = 1$ wt.% samples formed larger vesicles. This indicates that at low total lipid concentration ($C_{lp} = 0.3$ wt.%) at 10, 17 and 23 °C, the measured disk area at t_{final} agrees with the formation of ULVs with similar surface areas at both 0 mM and 3 mM [NaCl]. However, in the case of high total lipid concentration ($C_{lp} = 1$ wt.%) at 10 °C and 17 °C a significant amount of disk growth must occur after the measured annealing time. This is determined by comparing the difference in surface area between the last measured disk and the ULV, where there is a 9-11 fold increase in the absence of free salt and a 17-20 fold increase in the presence of free salt upon increasing temperature to 50 °C (Table 6.1.2.1).

Table 6.1.2.1. Summary of the average surface area of final disk measured and average surface area of resulting vesicle. Number of approximate disks required to form vesicles from the last average radius measured is represented by the $A_{vesicle}/A_{disk}$.

[NaCl]; C_{lp}	Disc Surface Area ($Å^2$)	Vesicle Surface Area ($Å^2$)	$A_{vesicle}/A_{disk}$
0 mM; 1wt%			
10-50 °C	1.29×10^5	1.42×10^6	11.0
17-50 °C	1.57×10^5	1.37×10^6	8.68
23-50 °C	5.33×10^5	1.27×10^6	2.39
3 mM; 1 wt%			
10-50 °C	1.72×10^5	3.41×10^6	19.8
17-50 °C	2.33×10^5	3.91×10^6	16.8
23-50C	$>1.83 \times 10^6$	$>1.71 \times 10^7$	NA
0 mM; 0.3 wt%			
10-50 °C	2.46×10^5	3.69×10^5	1.49
17-50 °C	2.88×10^5	3.54×10^5	1.22
23-50 °C	5.89×10^5	3.90×10^5	0.66
3 mM; 0.3 wt%			
10-50 °C	1.95×10^6	6.67×10^5	0.51
17-50 °C	6.80×10^5	8.47×10^5	1.24
23-50 °C	$>2.44 \times 10^6$	$>9.59 \times 10^6$	NA

6.2 DISCUSSION

6.2.1 Bicelle Growth

This study is an attempt to quantify bicelle growth as a function of time under different experimental conditions. In solution these particles collide and in the correct orientation, they stick together forming larger disks which are irreversible in size. This process can be visualized in Figure 6.2.1.1. These larger clusters continue to diffuse, collide and form even larger clusters up to a certain critical point, where they then become unstable and fold into ULVs with increasing temperature. Previously, two regimes; diffusion limited aggregation and reaction limited aggregation have been used to describe colloid aggregation [60], both of which we use to better comprehend the bicelle system under investigation. For simplicity, we assume the bicelle system to be comparable to colloids that in both cases the particles in solution undergo Brownian motion and experience inter-particle forces.

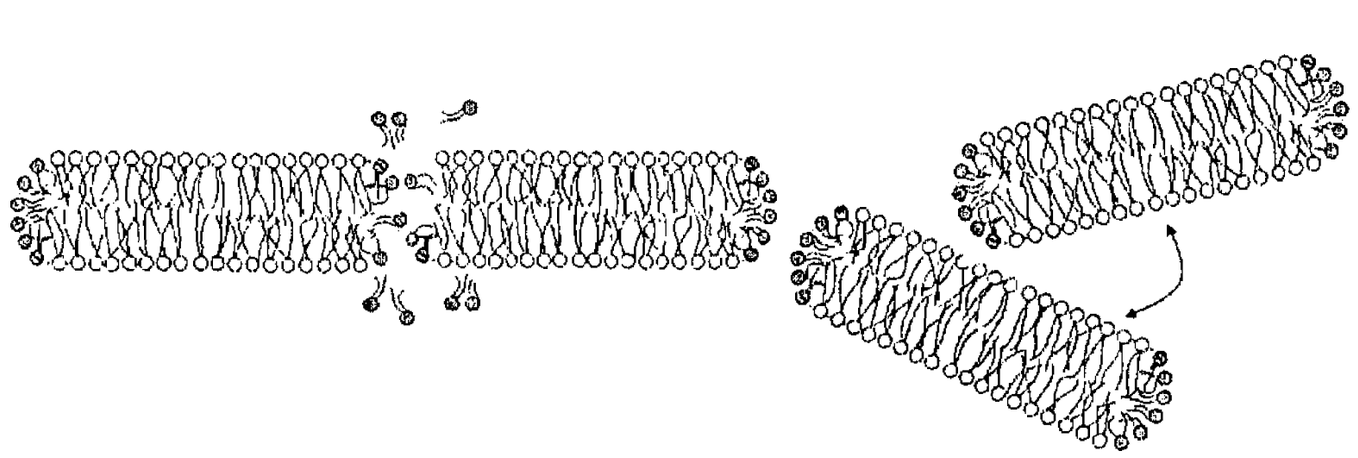

Figure 6.2.1.1. Bicelle coalescing at the edge-to-edge orientation where a loss of DHPC on the rims edge (gray lipids) contributes to the disk instability

The first regime describes the case of rapid aggregation where aggregation is limited by the time between collisions due to diffusion of particles. In this type of system, aggregation occurs immediately on contact and is a very fast process occurring over the course of seconds. Our experiments quantify bicelle growth over a period of hours, indicating that aggregation is not solely a result of diffusion and demonstrating a need for a more complex model to better understand the kinetics at hand [55, 57].

The slow aggregation rate we observed may imply that either the growth process is not completely diffusion controlled or multiple collisions may have to occur before two particles stick together. From Figure 6.2.1.1, it can be seen that only collisions in certain relative orientations (edge-to-edge) between bicelles are inelastic and lead to growth. This would result in a lower growth rate due to a decreased sticking probability as a function of the relative angle of collision. Lin et al. (1990) described this as being reaction limited aggregation where a number of collisions are needed before the particles bind due to interparticle forces [60, 61].

6.2.1.1 Temperature Dependent Growth

Previously it was assumed that below T_c, disks formed a stable state, with a constant disk radius (i.e. no growth). It was proposed that disk growth occurred solely upon increasing the temperature above T_c, entering the gel-liquid phase and leading to an increase in solubility of the DHPC in solution. This increase in DHPC solubility is said to result in a loss of the 'stabilizing' lipid on the edges of the disks, leading to coalescence with other disks [15]. Our results show bicelle growth to occur at temperatures less than and equal to T_c, indicating that in contrast to the previous hypothesis, destabilization of the edge from DHPC loss with increased solubility above T_c may not be the only possible mechanism to disk growth. The kinetic energy of the system even below T_c may be sufficient to destabilize the disks leading to disk growth.

Overall, temperature affects both the rate of particle diffusion as well as the repulsive energy of the system. It is noted that as temperature increases collision frequency also increases, (Figure 6.1.1.3). For samples of high lipid concentration (C_{lp} = 1 wt.%) both with and without the addition of free salt, we observe a significant increase in aggregation rate, most likely due to the decrease in the repulsion barrier or increase in collision frequency with increasing temperature (Figure 6.1.1.2). At C_{lp} = 0.3 wt.%, in the absence of free salt the principal role of temperature in controlling the rate of coalescing holds true, where we see an increase in growth rate with each increment of temperature. However, upon increasing the ionic strength of the solution the repulsion barrier is reduced by the free salt in solution and we observe a weaker temperature dependence at

lower temperatures of 10°C and 17°C where attractive van der Waals forces dominate the system as can be seen in Table 6.1.1.2 ([NaCl] = 3mM; C_{lp} = 0.3 wt.%).

6.2.1.2 Total Lipid Concentration Dependent Growth

Total lipid concentration affects two rate determining parameters controlling disk growth: collision frequency (result of diffusion) and disk stability. Under constant ionic strength and constant temperature conditions, the probability of two disks colliding will vary depending on interstitial disk spacing. With increasing total lipid concentration there is a decrease in spacing between disks, leading to an increase in the probability of disk collision. The increased disk collision frequency would result in an increase in disk growth; however our results indicate a slower growth rate and smaller disk size (Table 6.1.1.2). This can be understood in terms of the effect of C_{lp} on disk stability.

With an increase in total lipid concentration we see an increase in disk stability due to a greater amount of the stabilizing, short chain lipid (DHPC) coating the disk rim. This is better explained in terms of the critical micelle concentration (CMC) of the stabilizing lipid, DHPC (CMC = 1.4 mM). At C_{lp} = 0.3 wt.% the concentration of DHPC is below the CMC leading to increased solubility in D_2O. In contrast, at C_{lp} = 1 wt.% the DHPC content is well above the CMC indicating a greater amount of the short chain lipid at the disks' edge. Our results illustrate the dominant role of edge coverage (disk stability) in determining the growth rate which was previously identified in a similar system by Leng et al. (2003). Under fixed temperature conditions (17 and 23 °C) and at increased ionic strength (3 mM) the lower lipid concentration (C_{lp} = 0.3 wt.%) experiences significantly faster growth and is larger in size than the higher lipid concentration (C_{lp} = 1 wt.%), (refer to Figure 6.1.1.2a and 6.1.1.2b). The role of total lipid concentration in varying disk stability is further demonstrated by the fact that C_{lp} = 0.3 wt.% samples fold into ULVs sooner than C_{lp} = 1 wt.% samples. At t_{final}, for C_{lp} = 0.3 wt.% samples we see that disks are already in a state of instability transitioning to vesicles with comparable surface area ($A_{vesicles}$) to the precursor disk (A_{disk}) (Table 6.1.2.1). Furthermore, the increased disk stability for 1 wt.% samples contribute to further coalescing following the measured 23 °C t_{final} before closing into vesicles. Leng et al. (2002) and Egelhaap and Schurtenberger (1999) both report on the role of rapid dilution in the transformation of vesicles in a bile

salt system [16, 62]. They report that at greater dilutions (lower lipid concentration) the disks more readily fold up into vesicles of smaller radii than of lower dilutions (higher lipid concentration).

Furthermore we observe disk growth to slow down as disk size increases with time. This is best described by the decrease in total number of disks in solution and increase in amount of spacing between disks with growth.

6.2.1.3 Ionic Strength Dependent Growth

The screening effect of varying salt concentrations on Coulombic interactions on self-assembled charged systems has been previously reported with respect to the end-state vesicle properties where an increase in R_v is correlated with increasing free salt content [18, 63]. Our results are in accordance with these where we see a larger R_v with increased [NaCl] (from 0 to 3 mM) for both 0.3 and 1 wt.% samples at all annealing temperatures. Previously this effect was described by Winterhalter & Helfric (1988) where the addition of free salt decreases surface charge density and Debye length, resulting in a small, positive bending modulus and a negative Gaussian modulus, leading to a negative total elastic energy - favoring spontaneous vesiculation more readily [64]. In terms of bicelle interactions, we find that the rate of disk growth and the relative size of disks at a given time point is increased with increased ionic strength. Therefore the decrease in Debye length and surface charge density in the lower temperature regime favors more rapid aggregation. An even greater effect is seen in the low lipid concentration sample (0.3 wt.%) which is an already less stable system as discussed above.

6.2.2 Effect of Annealing on End-State ULV

Following the low temperature growth period all samples were heated to 50 °C and the disk-like morphologies closed to form vesicles. This disk-to-vesicle transition has been previously described to occur when the line tension at the disks rim increases with an increasing bending modulus and Gaussian modulus in the central region of the disk [65]. This depends on the size and energy of the disks where closure becomes more favorable as disk size increases. Here we attempt to explain the varying parameters and resulting disk closure based on the low temperature behavior studied.

C_{lp} and end-state vesicle: In the absence of NaCl, a larger end-state vesicle radius is observed with C_{lp} = 1 wt.% ($R_v \sim 200$ Å) in contrast to C_{lp} = 0.3 wt.%, ($R_v \sim 100$ Å). This effect of total lipid concentration on R_v is previously identified and discussed in the literature [18, 39, 62] where with increasing dilution disks close earlier, and smaller vesicles form. We find that for both C_{lp} = 0.3 wt.% and 1 wt.%, annealing temperature has no affect on R_v where the same sample annealed at 10, 17 and 23 °C are comparable in end-state vesicle size, indicating R_v to be independent of disk growth rate. We previously discussed the importance of disk stability and disk spacing in controlling disk growth rate which are also important in understanding disk closure. In the case of C_{lp} = 0.3 wt.% the final measured disk is comparable in surface area to the vesicle, $A_{vesicle}$ formed (Table 6.1.2.1). This indicates that even with an increase in sample temperature (following low temperature annealing), minimal disk interaction occurs prior to folding. We identify disk spacing to play a critical role where for C_{lp} = 0.3 wt.% disk spacing is already large, decreasing their chance to coalesce before folding. However, in the case of C_{lp} = 1 wt.% we see that $A_{vesicle}$ is significantly larger than A_{disk} at t_{final} in the case of 10 and 17 °C and 23 °C. We observe that for C_{lp} = 1 wt.% temperature is a limiting factor on disk size achievable where disk growth slows in the first few hours of annealing in all conditions (Figure 6.1.1.2). However further disk growth is known to occur after the measured time point due to the fact that disk spacing may not be at a maximum and neighboring disks may still be able to interact as temperature increases as is determined from the discrepancy in surface areas for C_{lp} = 1 wt.% samples (Table 6.1.2.1).

Ionic strength and end-state ULV: For constant dilution, electrostatic repulsion between disks is progressively screened upon increasing salt content, leading to faster growth [16]. Disks will thus grow further before they close which is what we observed where the addition of NaCl slightly increases the end-state ULV size. Furthermore we see that vesicle size slightly increases with increasing annealing temperature with the most significant effect seen at 23 °C annealing. This is best explained by the reduction in screening length between neighboring disks leading to an increase in the critical disk spacing where effective collisions are occurring at even further distances than in the case of no NaCl in which temperature can further facilitate growth.

Effect of Annealing on Polydispersity: When comparing the dependence of ULV polydispersity on sample composition we see a trend where lower lipid concentrations, increasing ionic strength and increasing annealing temperature slightly increases the polydispersity of the system, while for the most part still forming systems of relatively low polydispersity (Figure 6.1.2.2b). In general, the effect of polydispersity is most closely related to growth rate where increased growth rates are correlated with higher polydispersity systems. This indicates that faster growth rates may be correlated with non-uniform disk growth, which my lead to earlier vesiculation, especially at higher annealing temperatures, which would result in larger polydispersity.

CHAPTER 7
CONCLUSIONS, FUTURE WORK & RECOMENDATIONS

7.1 CONCLUSIONS

This thesis focused on the formation, optimization and characterization using SANS of ULVs.

The first section (Chapter 4) confirmed the formation of nano-sized vesicles composed of natural phospholipids in water under the following preparation conditions: low lipid concentrations (< 2 wt.%) and temperatures greater than T_c. Their spontaneous formation was successful. SANS results confirmed the formation of the precursor low temperature bicelle phase (~ 10 °C) and narrow size distribution of vesicles, $R_v \sim 75 \pm 5$ nm and $p \sim 0.13$ (~ 50 °C). Images obtained using cryo-TEM served as direct visualization of ULV formation and confirmation of the SANS results.

The second portion of research described in this thesis (Chapter 5) focused on controlling the size and size distribution of ULVs through varying the charge density and heating rate. Furthermore, the stability of the system was investigated as a function of total lipid concentration, C_{lp} to simulate environmental changes following intravenous injection. Spontaneously formed ULVs with low polydispersities ($p < 0.3$) were found in samples of [DMPG]/[DMPC] = 0.8 % and 1.5 %. Also a minimum charge density was necessary for the formation of ULVs, especially in the case of [DMPG]/[DMPC] = 0.3% samples, otherwise MLVs were formed. In addition, ULV size was shown to strongly correlate with bicelle folding which was controlled either through the amount of charge or the

period of time in which bicelles were permitted to coalesce into larger bicelles. Furthermore, through the interplay of charge density and thermal annealing protocol, ULV size is found to vary by as much as a factor of 6, revealing the possibility for the formation of a range of ULV sizes - depending on their application. Once formed, ULVs were stable following high temperature dilutions, verifying their insensitivity to C_{lp}.

The final portion of research described in this thesis (Chapter 6) involved a detailed study of the bicelle growth phase and its role in predicting the end-state ULV. These results demonstrated the dependence of bicelle growth on annealing temperature, ionic strength and total lipid concentration, all of which provided insight into the end-state properties of vesicles. It was found that the size of these nano-disks present in the low temperature regime increases continuously where their coalescence can be described by a power law model with time, based on the assumption of diffusion limited aggregation. The disk growth can be better explained conceptually by natural diffusion of particles in solution as well as interactive forces present, both of which affect collision frequency and collision efficiency. Overall, growth rate increased with increasing annealing temperature (10, 17 and 23 °C) and increasing ionic strength (0 versus 3 mM). A trend of increasing ULV size upon heating samples to 50 °C was also observed. However, this was not the case when comparing varying total lipid concentration where a decrease in bicelle growth rate and an increase in ULV size was associated with increasing C_{lp} (0.3 versus 1 wt.%), indicating that the rate of disk growth is not the only predictor of end-state properties but that disk spacing is also a critical factor.

This thesis shows that DMPC, DMPG and DHPC mixed in aqueous solution spontaneously form uniform, bilayered nano-disks (bicelles) below a critical temperature ($T_c \sim 23$ °C) which 'fold' into unilamellar vesicles (ULVs) upon elevating the temperature ($T > T_c$) which can be controlled effectively to meet various applications in drug delivery. The current method for creating self-assembled ULVs may be useful when it comes to producing these structures in industrial relevant quantities, which can then be used to great advantage in pharmaceutical applications.

7.2 Future Work And Recommendations

This work contributes to the basic research of spontaneously formed ULVs enhancing the general understanding and introducing novel methods for controlling their end-state properties. To date, research based on this system is focused on understanding and controlling the formation of the ULVs with little development towards their applications in the treatment of disease.

In order to validate this system as an effective drug delivery vehicle several more tests and experiments are required. One of the major experiments would be encapsulation of a molecule into the ULV core. As this work demonstrates, due to the self-assembling nature of these ULVs the formation may be affected by the inclusion of a new molecule. Therefore, it is recommended to confirm earlier results of size and polydispersity and potentially re-optimize the parameters for formation. Furthermore, determination of encapsulation efficiency and optimizing this is necessary. Following this, identifying the release kinetics as a function of temperature in a controlled environment, investigating cellular uptake, and the release kinetics *in vitro* are recommended.

Some common problems faced during drug delivery are rapid removal from the body prior to effectively treating desired regions of the body or failed delivery as previously mentioned in the literature review. The use of functionalization of the vesicle wall with PEG and/or with cell targeting ligands would be of great clinical relevance for improving circulation time and treatment efficacy – required for making a fully functional drug delivery vehicle.

In vivo experiments using an animal model are necessary to investigate the ability to control the release into specified areas of the body and further improve the specific treatment under investigation. Localized heating or cooling would be used to target release in the desired area. In summary, the specific areas of study should include: (1) circulation time of the encapsulated versus non-encapsulated molecules; (2) tracking of released agents in the body to verify if they are indeed localized by the use of a temperature trigger and (3) compare treatment efficacy as a function of dose rate when using ULVs.

REFERENCES

1. Goyal, P., Goyal, K., Vijaya Kumar, S.G., Singh, A., Katare, O.P., Mishra, D.N., *Liposomal drug delivery systems--clinical applications.* Acta Pharmaceutica, 2005. **55**(1): p. 1-25.

2. Wan, W.K., L. Yang, and D.T. Padavan, *Use of degradable and nondegradable nanomaterials for controlled release.* Nanomedicine, 2007. **2**(4): p. 483-509.

3. Allen, T.M. and P.R. Cullis, *Drug Delivery Systems: Entering the Mainstream.* Science, 2004. **303**(5665): p. 1818-1822.

4. Gregoriadis, G., *Targeting of Drugs.* Nature, 1977. **265**(5593): p. 407-411.

5. van der Graaf, S., C.G.P.H. Schroën, and R.M. Boom, *Preparation of double emulsions by membrane emulsification--a review.* Journal of Membrane Science, 2005. **251**(1-2): p. 7-15.

6. Olson, F., et al., *Preparation of liposomes of defined size distribution by extrusion through polycarbonate membranes.* Biochimica et Biophysica Acta (BBA) - Biomembranes, 1979. **557**(1): p. 9-23.

7. Szoka, F. and D. Papahadjopoulos, *Procedure for preparation of liposomes with large internal aqueous space and high capture by reverse-phase evaporation.* Proceedings of the National Academy of Sciences of the United States of America, 1978. **75**(9): p. 4194-4198.

8. Gregoriadis, G., *Engineering liposomes for drug delivery: progress and problems.* Trends in Biotechnology, 1995. **13**(12): p. 527-537.

9. Ollivon, M., et al., *Vesicle reconstitution from lipid-detergent mixed micelles.* Biochimica et Biophysica Acta (BBA) - Biomembranes, 2000. **1508**(1-2): p. 34-50.

10. Berger, N., et al., *Filter extrusion of liposomes using different devices: comparison of liposome size, encapsulation efficiency, and process characteristics.* International Journal of Pharmaceutics, 2001. **223**(1-2): p. 55-68.

11. Nieh, M.-P., et al., *SANS Study of the Structural Phases of Magnetically Alignable Lanthanide-Doped Phospholipid Mixtures.* Langmuir, 2001. **17**(9): p. 2629-2638.

12. Nieh, M.-P., et al., *Spontaneously Formed Unilamellar Vesicles with Path-Dependent Size Distribution.* Langmuir, 2005. **21**(15): p. 6656-6661.

13. Nieh, M.P., et al., *Concentration-Independent Spontaneously Forming Biomimetric Vesicles.* Physical Review Letters, 2003. **91**(15): p. 158105-158124.

14. Nieh, M.P., et al., *Spontaneously Formed Monodisperse Biomimetic Unilamellar Vesicles: The Effect of Charge, Dilution, and Time.* Biophysical Journal, 2004. **86**(4): p. 2615-2629.

15. Nieh, M.P., N. Kucerka, and J. Katsaras, *Spontaneously Formed Unilamellar Vesicles.* Methods in Enzymology Liposomes, Pt G, 2009. **465**: p. 3-20.

16. Leng, J., S.U. Egelhaaf, and M.E. Cates, *Kinetics of the Micelle-to-Vesicle Transition: Aqueous Lecithin-Bile Salt Mixtures.* Biophysical Journal, 2003. **85**(3): p. 1624-1646.

17. Nieh, M.-P., et al., *SANS Study on the Effect of Lanthanide Ions and Charged Lipids on the Morphology of Phospholipid Mixtures.* Biophysical Journal, 2002. **82**(5): p. 2487-2498.

18. Yue, B., et al., *Highly Stable Phospholipid Unilamellar Vesicles from Spontaneous Vesiculation:A DLS and SANS Study.* The Journal of Physical Chemistry B, 2004. **109**(1): p. 609-616.

19. Nieh, M.-P., J. Katsaras, and X. Qi, *Controlled release mechanisms of spontaneously forming unilamellar vesicles.* Biochimica et Biophysica Acta (BBA) - Biomembranes, 2008. **1778**(6): p. 1467-1471.

20. Mehnert, W. and K. Mäder, *Solid lipid nanoparticles: Production, characterization and applications.* Advanced Drug Delivery Reviews, 2001. **47**(2-3): p. 165-196.

21. Immordino, M.L., Dosio, F., Cattel, L., *Stealth liposomes: review of the basic science, rationale, and clinical applications, existing and potential.* International Journal of Nanomedicine 2006. **1**(3): p. 297–315.

22. Gabizon, A.A., *Pegylated Liposomal Doxorubicin: Metamorphosis of an Old Drug into a New Form of Chemotherapy.* Cancer Investigation, 2001. **19**(4): p. 424 - 436.

23. Drummond, D.C., et al., *Optimizing Liposomes for Delivery of Chemotherapeutic Agents to Solid Tumors.* Pharmacological Reviews, 1999. **51**(4): p. 691-744.

24. Maeda, H., et al., *Tumor vascular permeability and the EPR effect in macromolecular therapeutics: a review.* Journal of Controlled Release, 2000. **65**(1-2): p. 271-284.

25. Schiffelers, R., G. Storm, and I. Bakker-Woudenberg, *Liposome-encapsulated aminoglycosides in pre-clinical and clinical studies.* J. Antimicrob. Chemother., 2001. **48**(3): p. 333-344.

26. Vasey, P.A., et al., *Phase I Clinical and Pharmacokinetic Study of PK1 [N-(2-Hydroxypropyl)methacrylamide Copolymer Doxorubicin]: First Member of a New Class of Chemotherapeutic Agents—Drug-Polymer Conjugates.* Clinical Cancer Research, 1999. **5**(1): p. 83-94.

27. Senior, J. and G. Gregoriadis, *Stability of Small Unilamellar Liposomes in Serum and Clearance from the Circulation - the Effect of the Phospholipid and Cholesterol Components.* Life Sciences, 1982. **30**(24): p. 2123-2136.

28. Chithrani, B.D., A.A. Ghazani, and W.C.W. Chan, *Determining the Size and Shape Dependence of Gold Nanoparticle Uptake into Mammalian Cells.* Nano Letters, 2006. **6**(4): p. 662-668.

29. Yuan, F., et al., *Vascular Permeability in a Human Tumor Xenograft: Molecular Size Dependence and Cutoff Size.* Cancer Research, 1995. **55**(17): p. 3752-3756.

30. Bangham, A.D., M.M. Standish, and J.C. Watkins, *Diffusion of univalent ions across the lamellae of swollen phospholipids.* Journal of Molecular Biology, 1965. **13**(1): p. 238-252, IN26-IN27.

31. Johnson, S.M., et al., *Single bilayer liposomes.* Biochimica et Biophysica Acta (BBA) - Biomembranes, 1971. **233**(3): p. 820-826.

32. Klahn, J.K., et al., *On the escape process during phase inversion of an emulsion.* Colloids and Surfaces A: Physicochemical and Engineering Aspects, 2002. **210**(2-3): p. 167-181.

33. Ishii, F., A. Takamura, and H. Ogata, *Preparation conditions and evaluation of the stability of lipid vesicles (liposomes) using the microencapsulation technique.* Journal of Dispersion Science and Technology, 1988. **9**(1): p. 1 - 15.

34. Demé, B., et al., *Giant Collective Fluctuations of Charged Membranes at the Lamellar-to-Vesicle Unbinding Transition. 1. Characterization of a New Lipid Morphology by SANS, SAXS, and Electron Microscopy.* Langmuir, 2001. **18**(4): p. 997-1004.

35. Kaler, E., et al., *Spontaneous vesicle formation in aqueous mixtures of single-tailed surfactants.* Science, 1989. **245**(4924): p. 1371-1374.

36. Lesieur, P., et al., *Temperature-induced micelle to vesicle transition: kinetic effects in the DMPC/NaC system.* Journal of Applied Crystallography, 2000. **33**(3 Part 1): p. 623-627.

37. Safran, S.A., P. Pincus, and D. Andelman, *Theory of Spontaneous Vesicle Formation in Surfactant Mixtures.* Science, 1990. **248**(4953): p. 354-356.

38. Bergstrom, M., et al., *Small-Angle Neutron Scattering (SANS) Study of Vesicles and Lamellar Sheets Formed from Mixtures of an Anionic and a Cationic Surfactant.* The Journal of Physical Chemistry B, 1999. **103**(45): p. 9888-9897.

39. Nieh, M.-P., et al., *Spontaneously Forming Ellipsoidal Phospholipid Unilamellar Vesicles and Their Interactions with Helical Domains of Saposin C.* Langmuir, 2006. **22**(26): p. 11028-11033.

40. Fromherz, P., *Lipid-vesicle structure: Size control by edge-active agents.* Chemical Physics Letters, 1983. **94**(3): p. 259-266.

41. Katsaras, J., et al., *"Bicellar" Lipid Mixtures as used in Biochemical and Biophysical Studies.* Naturwissenschaften, 2005. **92**(8): p. 355-366.

42. Chen, S.H., *Small Angle Neutron Scattering Studies of the Structure and Interaction in Micellar and Microemulsion Systems.* Annual Review of Physical Chemistry, 1986. **37**(1): p. 351-399.

43. Perkins, S.J., *Structural studies of proteins by high-flux X-ray and neutron solution scattering.* Biochemical Journal, 1988. **254**: p. 313-327.

44. Willis, B.T.M., Carlile, C.J, *Experimental neutron scattering.* 2009, New York: Oxford University Press Inc.

45. Nieh, M.P., et al., *Adapting a triple-axis spectrometer for small angle neutron scattering measurements.* Review of Scientific Instruments, 2008. **79**(9): p. 095102 - 095102-6.

46. Glinka, C.J., et al., *The 30 m Small-Angle Neutron Scattering Instruments at the National Institute of Standards and Technology.* Journal of Applied Crystallography, 1998. **31**(3): p. 430-445.

47. Hayter, J.B. and J. Penfold, *An analytic structure factor for macroion solutions.* Molecular Physics: An International Journal at the Interface Between Chemistry and Physics, 1981. **42**(1): p. 109 - 118.

48. Feigin, L.A., Svergun, D.I., *Structure Analysis by Small-Angle X-Ray and Neutron Scattering.* Determination of the integral parameters of particles ed. G.W. Taylor. 1987, New York: Plenum Press.

49. Livsey, I., *Neutron-Scattering from Concentric Cylinders - Intraparticle Interference Function and Radius of Gyration.* Journal of the Chemical Society-Faraday Transactions Ii, 1987. **83**: p. 1445-1452.

50. Meuse, C.W., et al., *Hybrid bilayer membranes in air and water: Infrared spectroscopy and neutron reflectivity studies.* Biophysical Journal, 1998. **74**(3): p. 1388-1398.

51. Hayter, J.B., *Physics of Amphilphiles: Micelles, Vesicles and Microemulsions.* Determination of structure and dynamics of micellar solutions by neutron small angle scattering, ed. V. Degiorgio, Corti, M. 1985, Amsterdam: Elsevier Science.

52. Kline, S.R., *Reduction and analysis of SANS and USANS data using IGOR Pro.* Journal of Applied Crystallography, 2006. **39**: p. 895-900.

53. Kucerka, N., M.A. Kiselev, and P. Balgavy, *Determination of bilayer thickness and lipid surface area in unilamellar dimyristoylphosphatidylcholine vesicles from small-angle neutron scattering curves: a comparison of evaluation methods.* European Biophysics Journal with Biophysics Letters, 2004. **33**(4): p. 328-334.

54. Pozo-Navas, B., et al., *Discontinuous unbinding of lipid multibilayers.* Physical Review Letters, 2003. **91**(2): p. 028101-1-028101-4.

55. Lin, M.Y. and et al., *Universal diffusion-limited colloid aggregation.* Journal of Physics: Condensed Matter, 1990. **2**(13): p. 3093-3121.

56. Kofstad, P., *High-Temperature Oxidation of Metals*. 1966, New York: Wiley.

57. Sabın, J., et al., *Fractal aggregates induced by liposome-liposome interaction in the presence of Ca2+*. Eur. Phys. J. E, 2007. **24**(2): p. 201-210.

58. Sabín, J., G. Prieto, and F. Sarmiento, *Studying Colloidal Aggregation Using Liposomes*. 2010. p. 189-198.

59. Sabín, J., et al., *On the Effect of Ca2+ and La3+ on the Colloidal Stability of Liposomes.* Langmuir, 2005. **21**(24): p. 10968-10975.

60. Lin M Y, L.H.M., Weitz D A, Ball R C, Klein R and M. P, *Universality in colloid aggregation.* Nature, 1989. **339**(6223): p. 360-362.

61. Lin, M.Y., et al., *Universal reaction-limited colloid aggregation.* Physical Review A, 1990. **41**(4): p. 2005-2015.

62. Egelhaaf, S.U. and P. Schurtenberger, *Micelle-to-vesicle transition: A time-resolved structural study.* Physical Review Letters, 1999. **82**(13): p. 2804-2807.

63. Oberdisse, J., et al., *Vesicles and Onions from Charged Surfactant Bilayers:□ A Neutron Scattering Study.* Langmuir, 1996. **12**(5): p. 1212-1218.

64. Winterhalter, M. and W. Helfrich, *Effect of surface charge on the curvature elasticity of membranes.* The Journal of Physical Chemistry, 1988. **92**(24): p. 6865-6867.

65. Betterton, M.D. and M.P. Brenner, *Electrostatic Edge Instability of Lipid Membranes.* Physical Review Letters, 1999. **82**(7): p. 1598-1602.